

Error Control and Loss Functions for the Deep Learning Inversion of Borehole Resistivity Measurements

M. Shahriari^{1,2}, D. Pardo^{3,4,5}, J. A. Rivera^{3,4}, C. Torres-Verdín⁶,
A. Picon^{7,3}, J. Del Ser^{7,3,4}, S. Ossandón⁸, V. M. Calo⁹

¹ Software Competence Center Hagenberg (SCCH), Hagenberg, Austria.

² Euskampus Fundazioa, Bilbao, Spain.

³ University of the Basque Country (UPV/EHU), Leioa, Spain.

⁴ Basque Center for Applied Mathematics, (BCAM), Bilbao, Spain.

⁵ Ikerbasque (Basque Foundation for Sciences), Bilbao, Spain.

⁶ The University of Texas at Austin, USA.

⁷ Tecnia, Basque Research & Technology Alliance, 48170 Derio, Spain.

⁸ Pontificia Universidad Católica de Valparaíso, Valparaíso, Chile.

⁹ Curtin University, Perth, Australia.

Abstract

Deep learning (DL) can be employed as a numerical method to approximate functions. Recently, its use has become attractive for the simulation and inversion of multiple problems in computational mechanics, including the inversion of borehole logging measurements for oil and gas applications. In this context, DL methods exhibit two key attractive features: a) once trained, they enable to solve an inverse problem in a fraction of a second, which is convenient for borehole geosteering operations as well as in other real-time inversion applications. b) DL methods exhibit a superior capability for approximating highly-complex functions across different areas of knowledge. Nevertheless, as it occurs with most numerical methods, DL also relies on expert design decisions that are problem specific to achieve reliable and robust results. Herein, we investigate two key aspects of deep neural networks (DNNs) when applied to the inversion of borehole resistivity measurements: error control and adequate selection of the loss function. As we illustrate via theoretical considerations and extensive numerical experiments, these interrelated aspects are critical to recover accurate inversion results.

Keywords: logging-while-drilling (LWD), resistivity measurements, real-time inversion, deep learning, well geosteering, deep neural networks.

1. Introduction

In the last decade, deep learning (DL) algorithms have appealed to the masses due to their high performance in different applications, such as computer vision [1], speech recognition [2], and biometrics [3], to mention a few. In recent years, there have been significant advances in the field of DL, with

the appearance of residual neural networks (RNNs) [4], which prevent gradient degeneration during the training stage, and encoder-decoder (sequence-to-sequence) deep neural networks (DNNs), which have improved the DL work capability in computer vision applications [5]. Due to the high demand for DNNs from industry, dedicated libraries and packages such as Tensorflow [1], Keras [6], and Pytorch [7] have been developed. These libraries have facilitated the use of DNNs across different industrial applications [8–12]. All these advances combined make DNNs one of the most powerful and fast-growing artificial intelligence (AI) tools presently.

In this work, we focus on the application of DNNs to geosteering operations [13–15]. In this oil & gas application, a logging-while-drilling (LWD) instrument records electromagnetic measurements, which are inverted in real time to produce a map of the Earth’s subsurface. Based on the reconstructed Earth model, the operator adjusts the well-trajectory in real time to further explore exploitation targets, including oil & gas reservoirs, and to maximize the posterior productivity of the available reserves. Due to the tremendous productivity increase achieved with this technique, nowadays geosteering plays an essential role in the oil & gas industry [16].

The main difficulty one faces when dealing with geosteering problems is the real-time adjustment of the well trajectory. For that, we require a rapid inversion technique. Unfortunately, traditional inversion methods have severe limitations, which have forced geophysicists to look for novel solutions to this problem (see, e.g., [13–15, 17–21]). Gradient-based methods require simulating the forward problem dozens of times for each set of recorded measurements. Moreover, we need to also estimate the derivatives of the measurements with respect to the inversion variables, which is challenging and time consuming [22]. To alleviate the elevated computational costs associated with this inversion method, simplified 1.5-dimensional (1.5D) methods are routinely employed by oil companies (see, e.g., [14, 15, 23]). For the inversion of borehole resistivity measurements, it is also possible to apply statistics-based methods [24–26]. They perform forward simulations hundreds of times, which also require from large computational times [27]. Both gradient-based and statistics-based methods *only evaluate* the inverse operator. Thus, the entire inversion process is repeated at each new logging position.

The above limitations have forced geophysicists to look for novel methods. In here, we employ DNNs to approximate the inverse operator. Although the training stage of a DNN may be time consuming, after the network is properly trained, it can be evaluated in a fraction of a second [13]. This rapid inversion facilitates geosteering operations.

On the other side, DNNs also face important challenges when applied to the inversion of borehole resistivity problems. In particular, to properly train a DNN, we require a large dataset (also known as *ground truth*) with the solution of the forward problem for different Earth models [13, 28, 29]. Building a dataset may be time consuming, especially for two and three-dimensional problems. In those cases, we need to solve the forward problem using numerical simulation methods such as the finite element method (FEM) [23, 30, 31] or

the finite difference method (FDM) [32, 33]. Moreover, we need to optimize the sampling of the space that consists of the parameters describing all possible Earth models. Additionally, the training stage can be time consuming. However, this is an *offline* cost. One additional challenge arises due to the nature of inverse problems: they are not well-defined, i.e., there may exist multiple outputs for a given input [22, 27]. As we shall illustrate in this work, when using a DNN equipped with a traditional loss function based on the data misfit, the corresponding DNN approximations may be far away from any of the existing solutions to the inverse operator. This can seriously compromise the accuracy of the method and, consequently, the corresponding decision-making during geosteering operations.

In this work, we investigate the selection of the loss function to train a DNN when dealing with an inverse problem. We also introduce some error control during training. We focus on the inversion of borehole resistivity measurements. Nonetheless, most of the design decisions of such loss function are applicable to other inverse problems. To explain the main results stemming from this work, we first illustrate them with a simple mathematical example. Then, we apply the resulting DNN approximations to more challenging synthetic examples, which serve to analyze their main advantages and limitations. This work does not discuss the decision-making for the optimal selection of DNN architectures, nor an ideal data sampling technique for producing the datasets. Those subjects are considered as possible future works. However, for this article to be self-contained, we briefly describe in the appendix the architecture of the DNN we use.

The remainder of this article is organized as follows. Section 2 states the problem formulation. It also introduces two examples. In the first one, the exact solution of the inverse problem is the square root of the input data. This example serves to illustrate some of the main features and limitations of the proposed DL algorithms. The second example reproduces a realistic inversion scenario of borehole resistivity measurements. We also describe the selected parameterization of the Earth models. Section 3 describes the finite-dimensional input and output vector representations of the inverse operator that is approximated via DL. It also shows how we generate the ground truth dataset. Section 4 proposes a preprocessing of the input and output data variables so contributions to the loss (cost) function corresponding to different measurements and Earth parameters are comparable in magnitude. Section 5 describes the vector and matrix norms employed in this work, along with the corresponding absolute and relative errors. Section 6 analyzes various loss functions and illustrates their most prominent advantages and limitations. Section 7 describes the main implementation aspects of our DL inversion algorithm. Extensive numerical inversion results of borehole logging measurements are discussed in Section 8. In addition to some conclusions and future work described in Section 9, the manuscript also contains two appendices. Appendix A describes the borehole measurement acquisition system, including the employed logging instruments and recorded measurements. Appendix B details the selected DNN architectures.

2. Problem Formulation

2.1. Forward problem

We fix the measurement acquisition system $\tilde{\mathbf{s}}$. Then, for a well trajectory $\tilde{\mathbf{t}}$, and an Earth model $\tilde{\mathbf{p}}$, the forward problem consists of finding the corresponding borehole resistivity measurements $\tilde{\mathbf{m}}$. We denote by $\tilde{\mathcal{F}}$ the associated forward function. That is:

$$\tilde{\mathcal{F}}(\tilde{\mathbf{t}}, \tilde{\mathbf{p}}) = \tilde{\mathbf{m}}, \quad \text{where } \tilde{\mathbf{t}} \in \tilde{\mathbb{T}}, \tilde{\mathbf{p}} \in \tilde{\mathbb{P}}, \tilde{\mathbf{m}} \in \tilde{\mathbb{M}}. \quad (1)$$

In the above, we have omitted for convenience in the notation the dependence of function $\tilde{\mathcal{F}}$ upon the fixed input variable $\tilde{\mathbf{s}}$. $\tilde{\mathbb{P}}$ and $\tilde{\mathbb{M}}$ are normed vector spaces equipped with norms $\|\cdot\|_{\tilde{\mathbb{P}}}$ and $\|\cdot\|_{\tilde{\mathbb{M}}}$, respectively. $\tilde{\mathbb{T}}$ is also a vector space. Function $\tilde{\mathcal{F}}$ consists of a boundary value problem governed by Maxwell's equations (see [23] for details).

2.2. Inverse problem

In the inversion of borehole resistivity measurements, the objective is to determine the subsurface properties $\tilde{\mathbf{p}}$ corresponding to a set of measurements $\tilde{\mathbf{m}}$ recorded over a given trajectory $\tilde{\mathbf{t}}$. Again, the measurement acquisition system $\tilde{\mathbf{s}}$ is fixed. We denote that inverse operator as $\tilde{\mathcal{F}}^\dagger$ (pseudoinverse of $\tilde{\mathcal{F}}$). Mathematically, we have:

$$\tilde{\mathcal{F}}^\dagger(\tilde{\mathbf{t}}, \tilde{\mathbf{m}}) = \tilde{\mathbf{p}}, \quad \text{where } \tilde{\mathbf{t}} \in \tilde{\mathbb{T}}, \tilde{\mathbf{m}} \in \tilde{\mathbb{M}}, \tilde{\mathbf{p}} \in \tilde{\mathbb{P}}. \quad (2)$$

Again, we have omitted for convenience in the notation the dependence of function $\tilde{\mathcal{F}}^\dagger$ upon input variable $\tilde{\mathbf{s}}$. The governing physical equation of operator $\tilde{\mathcal{F}}^\dagger$ is unknown. However, it is known that a given input may have multiple associated outputs. Thus, such pseudoinverse function is not well-defined.

Figure 1 illustrates both forward and inverse problems.

2.3. Parameterization

We select a finite dimensional subspace of $\tilde{\mathbb{T}}$ parameterized with n_t real-valued numbers. The corresponding vector representation of an element from that subspace will be denoted by $\mathbf{t} \in \mathbb{R}^{n_t}$. We similarly parameterize a finite dimensional subspace of $\tilde{\mathbb{P}}$ and $\tilde{\mathbb{M}}$ with n_p and n_m real-valued numbers, respectively. The corresponding vector representations of an element from those subspaces will be denoted by $\mathbf{p} \in \mathbb{R}^{n_p}$ and $\mathbf{m} \in \mathbb{R}^{n_m}$, respectively.

The spans of vector representations \mathbf{p} and \mathbf{m} constitute two subspaces of \mathbb{R}^{n_p} and \mathbb{R}^{n_m} with norms $\|\cdot\|_{\mathbb{P}}$ and $\|\cdot\|_{\mathbb{M}}$, respectively. Ideally, these norms should be inherited from those associated with the original infinite dimensional spaces. However, this is often a challenging task and an open area of research. In here, we shall directly employ some existing (typically l_1 or l_2) finite dimensional norms.

Function \mathcal{F} will associate a pair (\mathbf{t}, \mathbf{p}) (vector representations of $(\tilde{\mathbf{t}}, \tilde{\mathbf{p}})$) with \mathbf{m} (vector representation of $\tilde{\mathbf{m}}$) such that $\mathcal{F}(\mathbf{t}, \mathbf{p}) = \mathbf{m}$. A similar notation will be employed for its pseudoinverse \mathcal{F}^\dagger acting on vector representations.

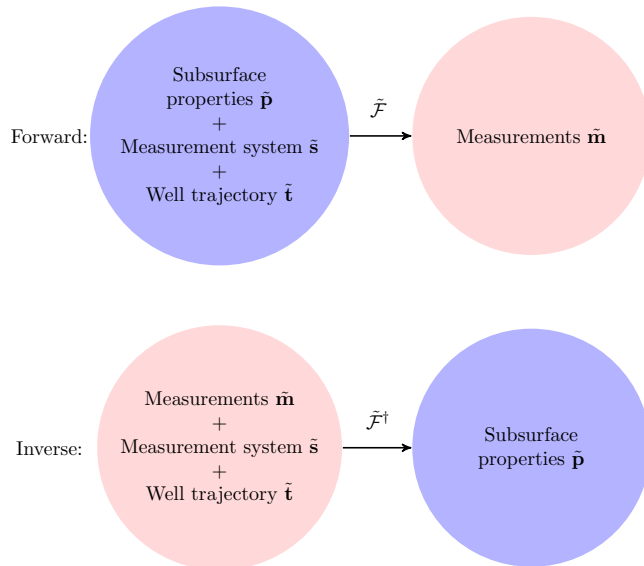


Figure 1: High-level description of a forward and an inverse problem.

To provide context and guidance for future developments, we introduce simple examples that illustrate some of the shortcomings of the standard techniques when applied to these problems, and we explain how we seek to overcome the associated challenges. The first problem seeks to predict the inverse of squaring a number. The second example focuses on geosteering applications.

2.4. Example A: Model problem with known analytical solution

We select $n_t = 0$, $n_p = n_m = 1$. The forward function is given by $\mathcal{F}(p) = p^2$, while the pseudoinverse has two solutions (branches): $\mathcal{F}^\dagger(m) = +\sqrt{m}$, and $\mathcal{F}^\dagger(m) = -\sqrt{m}$, as described in Figure 2.

This simple example contains a key feature exhibited by most inverse problems: it has multiple solutions. Thus, it illustrates the behaviour of DNNs when considering different loss functions. Results are enlightening and, as we shall see, they provide clear guidelines to construct proper loss functions for approximating inverse problems.

2.5. Example B: Inversion of borehole resistivity measurements

In geosteering applications, multiple oil and service companies perform inversion assuming a piecewise 1D layered model of the Earth. For that case, there exist semi-analytic methods that can simulate the forward problem in a

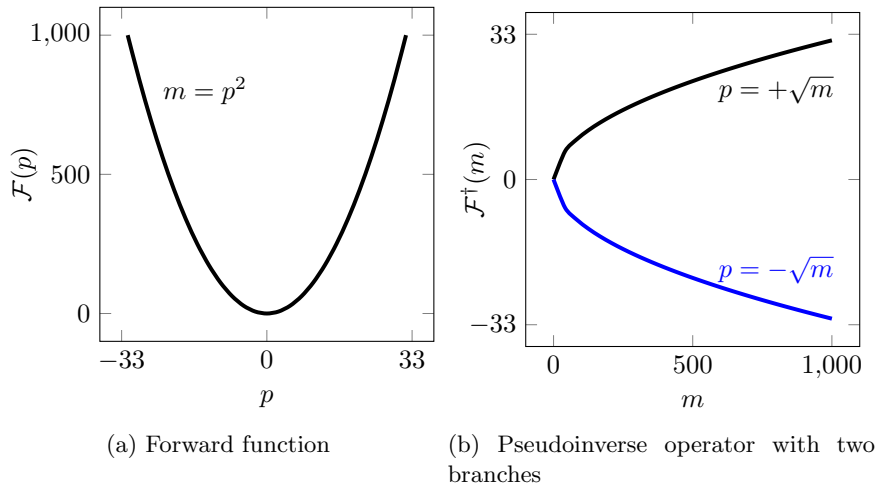


Figure 2: Model problem with known analytical solution.

fraction of a second. Herein, we use the same approach. Thus, the evaluation of \mathcal{F} is performed with a 1.5D semi-analytic code (see [23, 34]). As a result, at each logging position, our inversion operator recovers the formation properties of a 1D layered media [14, 15].

In the borehole resistivity applications considered in this work, we assume the Earth model to be a three-layer medium, as Figure 3 illustrates. A common practice in the field is to characterize this medium by seven parameters, namely: (a) ρ_h and ρ_v , the horizontal and vertical resistivities of the host layer, respectively; (b) ρ_u and ρ_l , the resistivities of the upper and lower isotropic layers, respectively; (c) d_u and d_l , the distances from the logging position to the upper and lower bed boundaries, respectively; and (d) β , the dipping angle of the formation. In this work, to simplify the problem, we consider only five of them by restricting the search to isotropic formations ($\rho_v = \rho_h$) with zero dip angle ($\beta = 0$). Thus, $n_p = 5$. In this example, we consider two cases (see Figure 4) according with different numbers of logging positions per data sample.

2.5.1. Example B.1: one logging position

For each sample, input measurements restrict to one logging position, which is the one used for the output (inverse results). In this case, $n_m = 6$.

2.5.2. Example B.2: 65 logging positions

For each sample, we select as input measurements those corresponding to a full logging trajectory formed by 65 logging positions. Thus, for each Earth model \mathbf{p} , we parameterize \mathbf{m} with 390 real numbers (i.e., $n_m = 390$).

Appendix A describes the logging instruments, positions, and post-processing system employed to record the measurements.

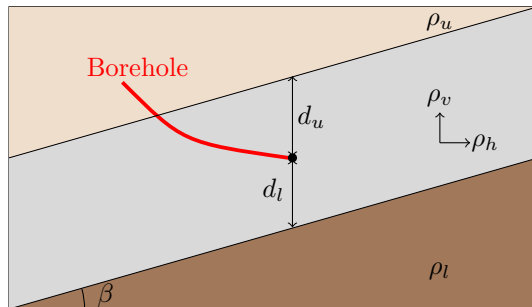
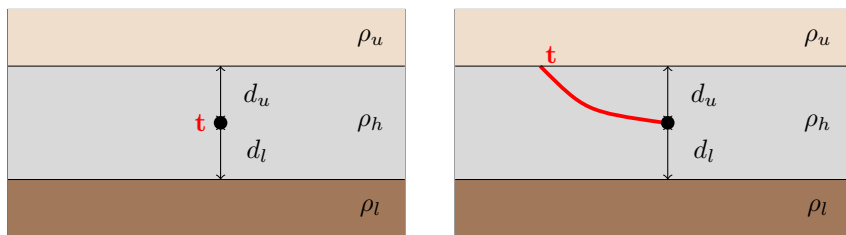


Figure 3: 1D media and a well trajectory. The black circle indicates the last trajectory position.



(a) Example B.1: trajectory with 1 logging positions

(b) Example B.2: trajectory with 65 logging positions

Figure 4: Model problems corresponding to examples B.1 and B.2, respectively.

3. Data Space and Ground Truth

In this work, we employ a DNN to approximate the discrete pseudoinverse operator \mathcal{F}^\dagger . Given a supervised database of n -pairs $(\mathbf{m}_i, \mathcal{F}^\dagger(\mathbf{t}_i, \mathbf{m}_i))$, $i = 1, \dots, n$, the DNN builds an approximation of the unknown function \mathcal{F}^\dagger . This section describes the construction of the supervised database.

We first select n and two subspaces of \mathbb{R}^{n_p} and \mathbb{R}^{n_t} , respectively. Then, we select n samples in those subspaces, namely, $((\mathbf{t}_1, \mathbf{p}_1), \dots, (\mathbf{t}_n, \mathbf{p}_n))$. To each of these samples, we apply the operator \mathcal{F} . That is, we compute $(\mathcal{F}(\mathbf{t}_1, \mathbf{p}_1), \dots, \mathcal{F}(\mathbf{t}_n, \mathbf{p}_n))$. Finally, the n -pairs $(\mathbf{m}_i, \mathcal{F}^\dagger(\mathbf{t}_i, \mathbf{m}_i)) := (\mathcal{F}(\mathbf{t}_i, \mathbf{p}_i), \mathbf{p}_i)$, $i = 1, \dots, n$ form our supervised database.

We denote by $\mathbf{T} \in \mathbb{R}^{n_t} \times \mathbb{R}^n$ to the set of all trajectory samples $(\mathbf{t}_1, \dots, \mathbf{t}_n)$. In other words, \mathbf{T} is a matrix with \mathbf{t}_i being its i -th column. Similarly, we define $\mathbf{M} = (\mathbf{m}_1, \dots, \mathbf{m}_n) \in \mathbb{R}^{n_m} \times \mathbb{R}^n$ and $\mathbf{P} = (\mathbf{p}_1, \dots, \mathbf{p}_n) \in \mathbb{R}^{n_p} \times \mathbb{R}^n$.

Example A: Simple model problem with known analytical solution. We select $n = 10^3$ uniformly spaced samples within the subspace $[-33, 33] \subset \mathbb{R}$.

Example B: Inversion of borehole resistivity measurements. We select $n = 10^6$. Then, for the five parameters described in Section 2.5, we select random samples

of the following rescaled variables over the corresponding intervals forming a subspace of \mathbb{R}^5 :

$$\begin{aligned} \log(\rho_l), \log(\rho_u), \log(\rho_h) &\in [0, 3] \\ \log(d_l), \log(d_u) &\in [-2, 1]. \end{aligned} \quad (3)$$

In this work we consider arbitrary high-angle trajectories that are parameterised via the following two variables:

$$\begin{aligned} \alpha_{ini} &\in [83^\circ, 97^\circ] \\ \alpha_v &\in [-0.045^\circ, 0.045^\circ] \quad (\text{only for Example B.2}), \end{aligned} \quad (4)$$

where α_{ini} is the initial trajectory dip angle and α_v is the variation of the dip angle at a given logging position with respect to the previous one. For each model problem, we randomly select the trajectory parameters within the above intervals. For Example B.1, $n_t = 1$, while for Example B.2, $n_t = 2$.

4. Data Preprocessing

Notation. For each output parameter of \mathcal{F} and \mathcal{F}^\dagger , we denote by $\mathbf{x} = (x_1, \dots, x_n)$ the n -samples associated with that parameter. Notice that x_i are real scalar values for $i = 1, \dots, n$. For example, in the borehole resistivity example, each variable \mathbf{x} contains n samples of each particular geophysical quantity such as resistivities, distances, or given measurements (attenuations, phases, etc.). Each dimension corresponds to a particular value (sample) of that variable, for example, the geosignal attenuation recorded at a specific logging position. From the algebraic point of view, the variable \mathbf{x} denotes a row of the matrices \mathbf{M} or \mathbf{P} .

Data preprocessing algorithm. It consists of three steps.

1. **Logarithmic change of coordinates.** We introduce the following change of variables:

$$\mathcal{R}_{\ln}(\mathbf{x}) := (\ln x_1, \dots, \ln x_n). \quad (5)$$

For some geophysical variables (e.g., the resistivity), it is convenient to perform such change of variables to ensure that equal-size relative errors will correspond to similar-size absolute errors. Thus, it is a change of variables intended to facilitate *local* (within a variable) comparisons.

2. **Remove outlier samples.** It often occurs that some outlier measurements may be present in the samples database. They may appear due to some measurement error or because of the physics of the problem. For example, in borehole resistivity measurements, some apparent resistivity measurements approach infinity, producing the so-called ‘‘horns’’ on the logs. When outlier measurements are present for any particular variable of the i -th sample x_i , then the entire sample should be removed. Otherwise, outlier measurements may affect the entire minimization problem, leading

to poor numerical results. The removal process may be automated using statistical indicators, or decided by the user on a priori physical knowledge about the problem. We follow this second approach in this work.

3. **Linear change of coordinates.** We now introduce a linear rescaling mapping into the interval $[0.5, 1.5]$. We select this interval since it has unit length and the mean of a normal (or a uniform) distribution variable \mathbf{x} is equal to one. Let $x_{\min} := \min_i x_i$, $x_{\max} := \max_i x_i$. We define:

$$\mathcal{R}_{lin}(\mathbf{x}) := \left(\frac{x_1 - x_{\min}}{x_{\max} - x_{\min}} + 0.5, \dots, \frac{x_n - x_{\min}}{x_{\max} - x_{\min}} + 0.5 \right). \quad (6)$$

In the above, limits x_{\min} and x_{\max} are fixed for all possible approximations \mathbf{x}^{app} . This change of variables allows us to perform a *global* comparison between errors corresponding to different variables since they all take values over the same interval.

Variables classification. We categorize each input and output geophysical variable \mathbf{x} into two types: *A* or *B*. When necessary, we shall indicate that a particular variable belongs to a specific category by adding the corresponding symbol as subindex of the variable, e.g., \mathbf{x}_A . Table 1 describes the domain of those variables as well as the rescaling employed for each of them. Variables of type *A* only require a global rescaling while those of type *B* require both a local and a global change of variables.

Geophysical Variables	Category	Domain	Rescaling
Angles, attenuations, phases, and geosignals	<i>A</i>	\mathbb{R}^n	$\mathcal{R}_{lin}(\mathbf{x})$
Apparent resistivities, resistivities, and distances	<i>B</i>	$(a, \infty)^n$ $a > 0$	$\mathcal{R}_{lin}(\mathcal{R}_{ln}(\mathbf{x}))$

Table 1: Categories for geophysical variables: types *A* or *B*. We apply a different rescaling to each of them.

For simplicity, we shall denote by \mathcal{R} the result of the above rescalings, i.e., $\mathcal{R}(\mathbf{x}_A) := \mathcal{R}_{lin}(\mathbf{x}_A)$, and $\mathcal{R}(\mathbf{x}_B) := \mathcal{R}_{lin}(\mathcal{R}_{ln}(\mathbf{x}_B))$. In general, given a variable \mathbf{x} (of category *A* or *B*), we represent $\mathbf{x}_{\mathcal{R}} := \mathcal{R}(\mathbf{x})$. Given a matrix $\mathbf{X} \in \mathbb{R}^{n_x} \times \mathbb{R}^n$, we abuse notation and denote by $\mathbf{X}_{\mathcal{R}} := \mathcal{R}(\mathbf{X}) \in \mathbb{R}^{n_x} \times \mathbb{R}^n$ to the matrix that results from applying operator \mathcal{R} rowwise.

Remark: Substituting in Equation 5 the Napierian logarithm for the base ten logarithm does not affect the definition of \mathcal{R} . Results are identical.

5. Norms and Errors

We first introduce both the vector and the matrix norms that we will use during the training process.

Vector norms. We introduce a norm $\|\cdot\|_{\mathbb{X}}$ associated with variable \mathbf{x} . In general, we will employ the l_1 or l_2 norms given by:

$$\begin{aligned}\|\mathbf{x}\|_1 &= \sum_{i=1}^n |x_i|, \\ \|\mathbf{x}\|_2 &= \sqrt{\sum_{i=1}^n |x_i|^2}.\end{aligned}\tag{7}$$

Matrix norms. We introduce a norm $\|\cdot\|_X$ associated with matrix $\mathbf{X} = (x_{ij}) \in \mathbb{R}^{n_x} \times \mathbb{R}^n$. We consider an “entrywise norm” of the type $l_{p,q}$ for some $p, q \geq 1$ defined for a matrix \mathbf{X} as (see [35]):

$$\|\mathbf{X}\|_{p,q} := \left(\sum_{i=1}^{n_x} \left(\sum_{j=1}^n |x_{ij}|^q \right)^{\frac{p}{q}} \right)^{\frac{1}{p}}.\tag{8}$$

In this work, we employ the $l_{1,1}$ and $l_{2,2}$ norms. Notice that the $l_{2,2}$ norm is the Frobenius norm.

Absolute and relative errors. Let $\mathbf{x}^{app} = (x_1^{app}, \dots, x_n^{app})$ be an approximation of \mathbf{x} . We define the absolute error A_e between \mathbf{x}^{app} and \mathbf{x} in the $\|\cdot\|_{\mathbb{X}}$ norm as

$$A_e^{\mathbb{X}}(\mathbf{x}^{app}, \mathbf{x}) := \|\mathbf{x}^{app} - \mathbf{x}\|_{\mathbb{X}}.\tag{9}$$

Similarly, for a matrix \mathbf{X} and its approximation \mathbf{X}^{app} , we define:

$$A_e^X(\mathbf{X}^{app}, \mathbf{X}) := \|\mathbf{X}^{app} - \mathbf{X}\|_X.\tag{10}$$

This error measure has limited use since it is challenging to select an absolute error threshold that distinguishes between a *good* and a *bad* quality approximation. To overcome this issue, practitioners often employ relative errors. We define the relative error R_e in percent between \mathbf{x}^{app} and \mathbf{x} in the $\|\cdot\|_{\mathbb{X}}$ norm as:

$$R_e^{\mathbb{X}}(\mathbf{x}^{app}, \mathbf{x}) := 100 \frac{\|\mathbf{x}^{app} - \mathbf{x}\|_{\mathbb{X}}}{\|\mathbf{x}\|_{\mathbb{X}}}.\tag{11}$$

Similarly, for matrices we define:

$$R_e^X(\mathbf{X}^{app}, \mathbf{X}) := 100 \frac{\|\mathbf{X}^{app} - \mathbf{X}\|_X}{\|\mathbf{X}\|_X}.\tag{12}$$

Error control. For a variable \mathbf{x} and its approximation \mathbf{x}^{app} , we want to control the relative error of the rescaled variable, that is:

$$R_e^{\mathbb{X}}(\mathbf{x}_{\mathcal{R}}^{app}, \mathbf{x}_{\mathcal{R}}).\tag{13}$$

The value $\|\mathbf{x}_{\mathcal{R}}\|_{\mathbb{X}}$ is expected to be similar for all variables \mathbf{x} . Thus, the minimizer of the sum over the existing variables of the absolute errors $A_e^{\mathbb{X}}(\mathbf{x}_{\mathcal{R}}^{app}, \mathbf{x}_{\mathcal{R}})$ should provide almost optimal results in terms of minimizing the sum of relative errors.

6. Loss Function

In this section, we consider a set of weights $\theta \in \Theta$ and a function $\mathcal{F}_{\mathcal{R},\theta}^\dagger$ that depend upon the selected DNN architecture (see Appendix B). Then, we introduce a loss function that depends of $\mathcal{F}_{\mathcal{R},\theta}^\dagger$. We denote as $\mathcal{F}_{\mathcal{R},\theta^*}^\dagger$ to the minimizer of the loss function over all possible weight sets. Function $\mathcal{F}_{\theta^*}^\dagger := \mathcal{R}^{-1} \circ \mathcal{F}_{\mathcal{R},\theta^*}^\dagger \circ \mathcal{R}$ is the final DNN approximation of \mathcal{F}^\dagger . By repeating this process with different loss functions, we analyze the advantages and limitations of each one.

6.1. Data misfit

A simple loss function (and the corresponding optimization problem) based on the data misfit is given by:

$$\mathcal{F}_{\mathcal{R},\theta^*}^\dagger := \arg \min_{\theta \in \Theta} \|\mathcal{F}_{\mathcal{R},\theta}^\dagger(\mathbf{T}_{\mathcal{R}}, \mathbf{M}_{\mathcal{R}}) - \mathbf{P}_{\mathcal{R}}\|_P. \quad (14)$$

In the above equation, symbol $\|\cdot\|_P$ indicates a matrix norm of the type introduced in Section 5.

6.1.1. Example A: Model problem with known analytical solution

In this example, $n_p = 1$. Thus, matrix norms reduce to vector norms. Figure 5 illustrates the results we obtain using the l_1 and l_2 norms, respectively. These disappointing results are expected. Indeed, for the l_2 -norm, it is easy to show that for a sufficiently flexible DNN architecture, the exact solution is $\mathcal{F}_{\theta^*}^\dagger \approx 0$. To prove this, we assume that for every sample of the form (m, \sqrt{m}) , there exist another one $(m, -\sqrt{m})$, which is satisfied in our dataset by construction (see Section 3). Then, for each pair of samples of this form, the exact point that minimizes the distance between both solutions (\sqrt{m} and $-\sqrt{m}$) is 0. This argument can be extended to all pairs of samples. A similar reasoning shows that for the l_1 -norm, any solution in between the two square root branches is an exact solution of the inverse problem. Our numerical solutions in Figure 5 confirm these simple mathematical observations. Thus, the data misfit loss function is unsuitable for inversion purposes.

6.2. Misfit of the measurements

To overcome the aforementioned limitation, it is possible to consider the following loss function that measures the misfit of the measurements (see [36]):

$$\mathcal{F}_{\mathcal{R},\theta^*}^\dagger := \arg \min_{\theta \in \Theta} \|(\mathcal{F}_{\mathcal{R}} \circ \mathcal{F}_{\mathcal{R},\theta}^\dagger)(\mathbf{T}_{\mathcal{R}}, \mathbf{M}_{\mathcal{R}}) - \mathbf{M}_{\mathcal{R}}\|_M, \quad (15)$$

where $\mathcal{F}_{\mathcal{R}} := \mathcal{R} \circ \mathcal{F} \circ \mathcal{R}^{-1}$, and $\|\cdot\|_M$ indicates a matrix norm of the type introduced in Section 5.

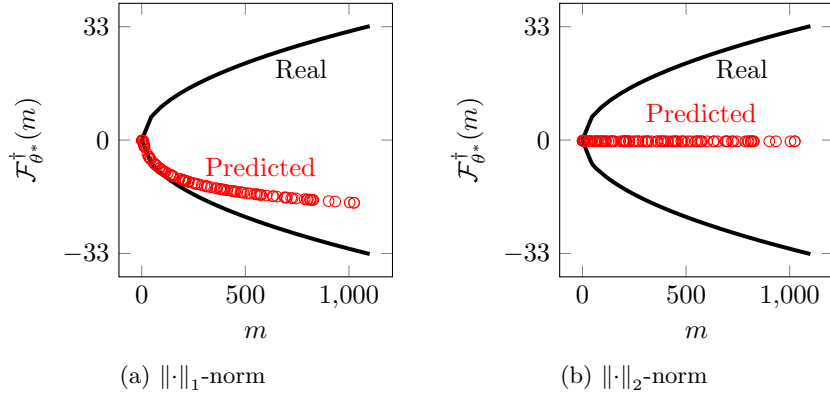


Figure 5: Analytical solution vs DNN predicted solution evaluated over the test dataset using the loss function based on the data misfit.

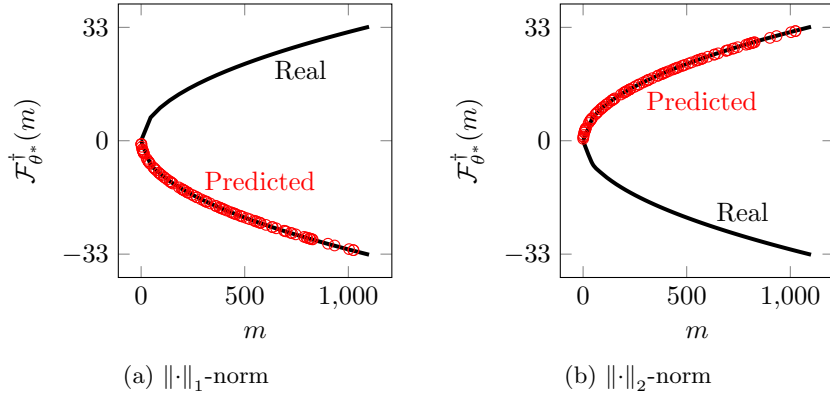


Figure 6: Analytical solution vs DNN predicted solution evaluated over the test dataset using the loss function based on the measurements misfit.

Example A: Model problem with known analytical solution. Figure 6 shows the inversion results when using the misfit of the measurements. We recover one of the possible solutions of the inverse operator. A regularization term could be introduced to select one solution branch over the other.

Despite the accurate results exhibited for the above example, the proposed loss function has some critical limitations that affect its performance. Namely, during training, it is necessary to evaluate the forward problem multiple times. Depending upon the size of the training dataset and number of iterations required to converge, this may lead to millions of forward function evaluations. Solving the forward problem for such large number of times is time-consuming even with a 1.5D semi-analytic simulator. Moreover, most forward solvers are implemented for CPU architectures, while the training of the DNN normally occurs on GPUs. This requires a permanent communication between GPU and CPU, which further slows down the training process. Porting the forward solver

\mathcal{F} to a GPU may be complex to implement and bring additional numerical difficulties.

6.3. Encoder-decoder

To overcome the aforementioned implementation challenges, we propose to approximate the forward function using another DNN \mathcal{F}_{ϕ^*} , where $\phi^* \in \Phi$ are the parameters associated to the trained DNN. With this approach, we simultaneously train the forward and inverse operators solving the following optimization problem:

$$(\mathcal{F}_{\mathcal{R},\phi^*}, \mathcal{F}_{\mathcal{R},\theta^*}^\dagger) := \arg \min_{\phi \in \Phi, \theta \in \Theta} \{ \|(\mathcal{F}_{\mathcal{R},\phi} \circ \mathcal{F}_{\mathcal{R},\theta}^\dagger)(\mathbf{T}_{\mathcal{R}}, \mathbf{M}_{\mathcal{R}}) - \mathbf{M}_{\mathcal{R}}\|_M + \|\mathcal{F}_{\mathcal{R},\phi}(\mathbf{T}_{\mathcal{R}}, \mathbf{P}_{\mathcal{R}}) - \mathbf{M}_{\mathcal{R}}\|_M \}, \quad (16)$$

Function $\mathcal{F}_{\phi^*} := \mathcal{R}^{-1} \circ \mathcal{F}_{\mathcal{R},\phi^*} \circ \mathcal{R}$ is the final DNN approximation to \mathcal{F} . The first term in the above loss function constitutes an encoder-decoder DNN architecture [5] and ensures that function $\mathcal{F}_{\mathcal{R},\theta^*}^\dagger$ shall be a pseudoinverse of $\mathcal{F}_{\mathcal{R},\phi^*}$. The second term imposes that the forward DNN approximates the ground truth data. In particular, it prevents situations in which both $\mathcal{F}_{\mathcal{R},\theta^*}^\dagger$ and $\mathcal{F}_{\mathcal{R},\phi^*}$ approximate the identity operator.

Example A: Model problem with known analytical solution. Figure 7 shows the results obtained with the encoder-decoder loss function. We recover accurate inversion results.

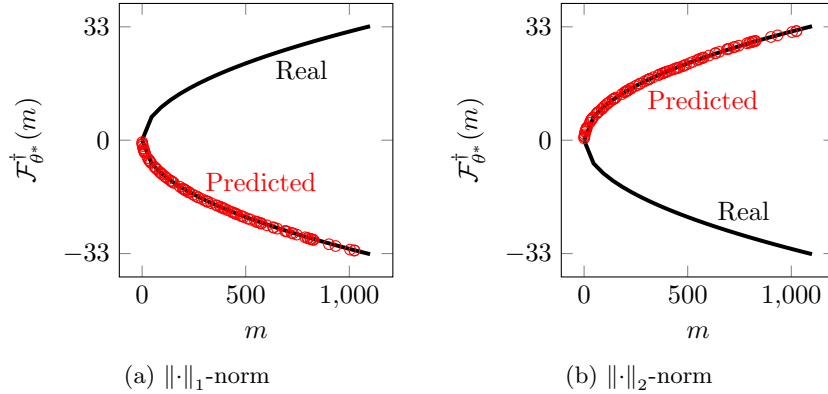


Figure 7: Analytical solution vs DNN predicted solution evaluated over the test dataset using the encoder-decoder loss function.

6.4. Two-steps approach

It is possible to decompose the above encoder-decoder based loss function into two step: the first one intended to approximate the forward function, and

the second one to determine the pseudoinverse operator:

$$\begin{aligned}\mathcal{F}_{\mathcal{R},\phi^*} &:= \arg \min_{\phi \in \Phi} \|\mathcal{F}_{\mathcal{R},\phi}(\mathbf{T}_{\mathcal{R}}, \mathbf{P}_{\mathcal{R}}) - \mathbf{M}_{\mathcal{R}}\|_M, \\ \mathcal{F}_{\mathcal{R},\theta^*}^\dagger &:= \arg \min_{\theta \in \Theta} \|(\mathcal{F}_{\mathcal{R},\phi^*} \circ \mathcal{F}_{\mathcal{R},\theta}^\dagger)(\mathbf{T}_{\mathcal{R}}, \mathbf{M}_{\mathcal{R}}) - \mathbf{M}_{\mathcal{R}}\|_M.\end{aligned}\tag{17}$$

Example A: Model problem with known analytical solution. Figure 8 shows the results of the inversion using the two-steps approach. We recover a faithful approximation of the inverse operator.

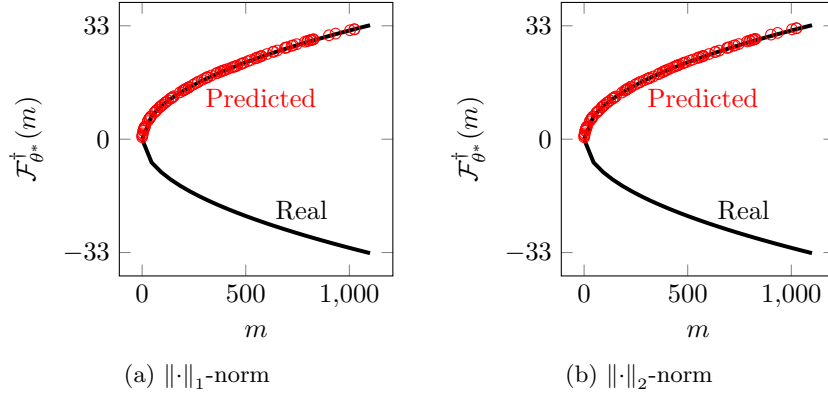


Figure 8: Analytical solution vs DNN predicted solution evaluated over the test dataset using the two-step loss function.

Remark A: Based on the above discussion, it may seem that loss functions given by Equations 16 or 17 are ideal to solve inverse problems. However, there is a critical issue that needs to be addressed. In Equation 17a, the forward DNN $\mathcal{F}_{\mathcal{R},\phi}$ is trained only for the given dataset samples. However, it may (and often will) occur that the the output of the DNN approximation of the pseudo-inverse operator $\mathcal{F}_{\mathcal{R},\theta}^\dagger$ will deliver data far away from the data space used to produce the training samples. This may lead to catastrophic results. To illustrate this, we consider our model problem with known analytical solution. If we consider a dataset with only positive values of p , then the following approximations will lead to a zero loss function:

$$\mathcal{F}_{\phi^*}(p) = \begin{cases} p^2 & \text{if } p > 0 \\ ap^2 & \text{if } p < 0 \end{cases} \quad \mathcal{F}_{\theta^*}^\dagger(m) = -\sqrt{m/a},\tag{18}$$

for any $a > 0$. However, if $a \neq 1$, this approximation is far away from any of our two original solutions of the inverse problem. To prevent these undesired situations, one needs to ensure that the output space of $\mathcal{F}_{\mathcal{R},\theta^*}$ is sufficiently close to the space from which we obtain the training samples.

6.5. Regularization term

Inverse problems often exhibit non-unique solutions. Thus, in numerical methods, it is often typical to introduce some regularization term aiming at selecting a particular desired solution out of all the existing ones.

In DL applications, most regularization techniques operate on the model architecture (e.g., by penalizing high-valued weights). In here, we propose a regularization term based on adding the term given by the loss function of Equation 14 measured in the l_1 -norm to either the loss function given by Equation 16 or 17b. This guides the solution towards the ones considered in the training dataset, which may be convenient. At the same time, such regularization term often hides the fact that other very different solutions of the inverse problem may coexist. We will study the advantages and limitations of including this regularization term in detail in Section 8.

7. Implementation

To solve the forward problem, we employ a semi-analytic method [34] implemented in Fortran 90 [23]. With it, we produce a dataset containing one million samples (*ground truth*). Each sample consists of a randomly selected 1D layered model (see Section 3 for details). We use 80% of the samples for training the DNNs, 10% for validating them, and the remaining 10% for testing.

We consider two DNN architectures to approximate \mathcal{F} and \mathcal{F}^\dagger , respectively. The forward function \mathcal{F} is well-defined and continuous, while the inverse operator \mathcal{F}^\dagger is not even well-defined. Thus, we employ a simpler DNN architecture to approximate \mathcal{F} than that employed to approximate \mathcal{F}^\dagger . See Appendix B for details.

We implement our DNNs using *Tensorflow 2.0* [37] and *Keras* [6] libraries. To train the DNNs, we use a *NVIDIA Quadro GV100* GPU. Using this hardware device, we require almost 70 hours to simultaneously train $\mathcal{F}_{\mathcal{R},\phi^*}$ and $\mathcal{F}_{\mathcal{R},\theta^*}^\dagger$. While the training process is time-consuming, it is performed *offline*. Then, the *online* part of the process consists of simply evaluating the DNN, which can deliver an inverse model for thousands of logging positions in few seconds. This low *online* computational cost makes the DNN approach an excellent candidate to perform inversion during geosteering operations in the field.

8. Numerical Results

We perform a three step evaluation process of the results:

1. The first one consists of studying the evolution of each term in the loss function during the training process. This analysis assesses the overall performance of the training process and, in particular, it shows if any particular term of the loss function is driving the optimization procedure in detriment of other terms.
2. Second, we produce multiple cross-plots, which provide essential information about the adequacy of the selected loss function and dataset. It also indicates the possible non-uniqueness of the inverse problem at hand.
3. Finally, we apply the trained networks to invert three realistic synthetic models and analyze the overall success of the proposed DNN algorithm as well as its limitations.

The above evaluation process provides an step-by-step assessment of the adequacy of the proposed strategy for solving inverse problems.

In most cases, we observe similar results when we consider the encoder-decoder loss function given by Equation 16 and the two-step loss function given by Equation 17. For brevity on the exposition, most of the results shown here correspond to the encoder-decoder. Additionally, we include one set of results using the two-step loss function, for which the observed behaviour is essentially different from that of the encoder-decoder.

8.1. Evolution of the loss function

Figure 9 displays the evolution of the terms composing the encoder-decoder loss function described in Equation 16 for the Example B.1. Figure 10 displays the corresponding results when we add the regularization term based on Equation 14. In both figures, we observe: (a) a proper reduction of the total loss function, indicating that the overall minimization process has been successful; (b) an adequate balance between the loss contribution of the different terms composing each loss function, suggesting that all terms of the loss functions have been simultaneously minimized; and (c) a satisfactory match between the loss functions corresponding to the training and the validation data samples, which indicates we have prevented overfitting. Similar results are observed with Example B.2, which we skip here for brevity. Results per variable are also omitted since the applied rescaling described in Section 4 guarantees a good balance between different variables.

8.2. Cross-plots

We consider the following types of cross-plots:

$$\begin{aligned}
 \text{Cross-plot 1: } & \mathcal{F} \circ \mathcal{F}^\dagger \quad vs \quad \mathcal{F}_{\phi^*} \circ \mathcal{F}^\dagger \\
 \text{Cross-plot 2: } & \mathcal{F} \circ \mathcal{F}^\dagger \quad vs \quad \mathcal{F}_{\phi^*} \circ \mathcal{F}_{\theta^*}^\dagger \\
 \text{Cross-plot 3: } & \mathcal{F} \circ \mathcal{F}^\dagger \quad vs \quad \mathcal{F} \circ \mathcal{F}_{\theta^*}^\dagger \\
 \text{Cross-plot 4: } & \mathcal{F}^\dagger \quad vs \quad \mathcal{F}_{\theta^*}^\dagger
 \end{aligned} \tag{19}$$

In the above, \mathcal{F} and \mathcal{F}^\dagger are the exact functions and they define the *ground truth*, while the others are the *predictions*. Notice that for the first three types of cross-plots, the ground truth is simply the identity mapping. Each type of cross-plot can be displayed for the training, validation, and test data samples and for each variable. In our Example B, this makes a total of 69 cross-plots. In addition, we need to repeat them for each considered loss function. To compress this information, we quantify each cross-plot with a single number: the statistical measure *R*-squared (R^2), which represents how much variation of the ground truth is explained by the predicted value. When this value is close to 1, indicating a perfect matching between the predicted value and the ground truth, cross-plots can be often safely omitted. Otherwise, cross-plots may display interesting information beyond that provided by R^2 .

Proper interpretation of the cross-plots (or alternatively, R^2 factors) is of upmost importance. Cross-plots of type 1 (Equation 19₁) indicate how well the

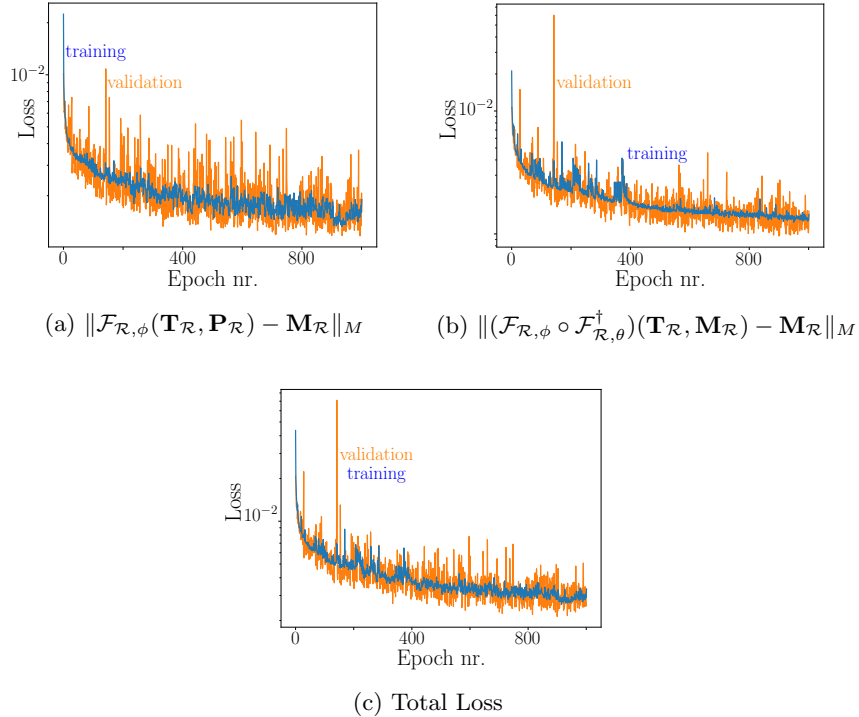


Figure 9: Example B.1. Evolution of the different terms of the encoder-decoder loss function given by Equation 16 without regularization.

forward function is approximated over the given dataset. Cross-plots of type 2 (Equation 19₂) display how well the composition of the predicted forward and inverse mappings approximate the identity. These two types of cross-plots often deliver high R^2 factors, since the corresponding approximations are directly built into the encoder-decoder loss function given by Equation 16. Table 2 confirms those theoretical predictions for the most part.

A further in-depth inspection of Table 2 reveals that for the the geosignal measurements (both attenuation and phase) corresponding to Example B.1 without regularization, cross-plots 2 exhibit significantly better R^2 factors than those corresponding to cross-plots 1. Figure 11 shows the corresponding cross-plots. The anti-diagonal grey line forming in cross-plots of type 1 corresponds to dip angles of the logging instrument very close to 90 degrees. At that angle, the geosignal is discontinuous (see Appendix A). Thus, it is not properly approximated via DL algorithms, which are designed to approximate continuous functions. Cross-plots of type 2 seem to fix that issue by delivering higher R^2 factors and apparently nicer figures. However, they are amplifying the problem and hiding it, since what it is really occurring is that the DL approximation of the pseudo-inverse operator is perfectly inverting an incorrect forward approxi-

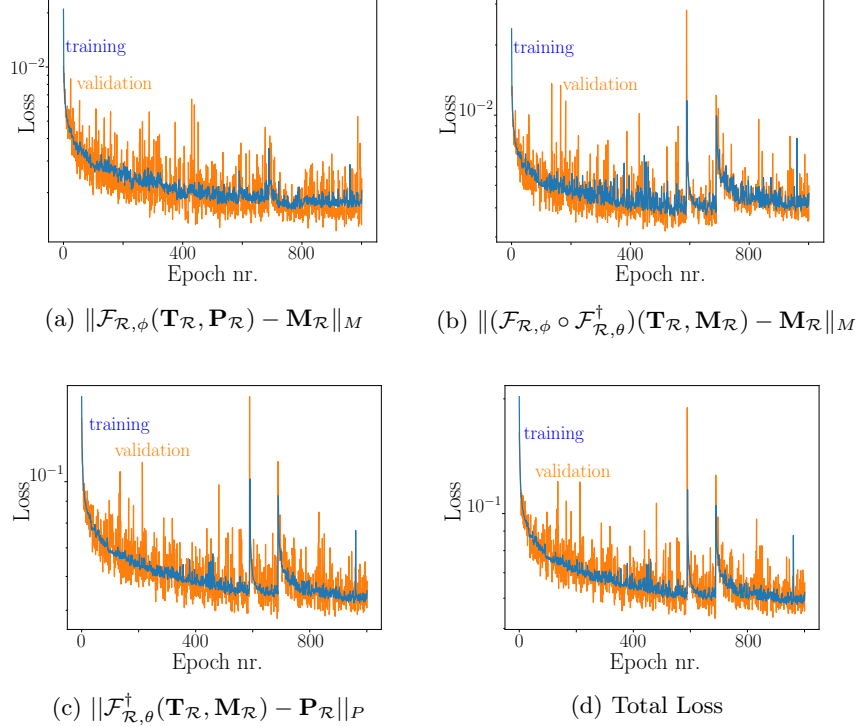


Figure 10: Example B.1. Evolution of the different terms of the encoder-decoder loss function given by Equation 16 with the regularization term prescribed by Equation 14.

mation. Numerical results shown later in this Section will further illustrate this problem.

Obtaining high R^2 factors associated to cross-plots of type 3 (Equation 19₃) is a much more challenging task due to Remark A of Section 6. Equation 18 shows a simple example in which cross-plots of type 1 and 2 deliver perfect R^2 marks and results, while cross-plots of type 3 are disastrous. This is also the situation that occurs in Example B.2. (see Table 3). While the original training dataset is based on 1D Earth models, the one obtained after the predicted DNN inversion is a *piecewise* 1D Earth model, for which \mathcal{F}_{ϕ^*} is untrained for. When this occurs, the training database should be upgraded, either by increasing the space of the data samples or by selecting a different parameterization (e.g., measurements) for each sample. In our case, we follow this later strategy, and we move to Example B.1.

Table 3 shows mixed results for Example B.1. Results without regularization are unspectacular with the geosignal exhibiting poor results. The DNN pseudo-inverse approximation inverts accurately the DNN forward approximation, but not the true forward function. Again, this occurs because the DNN pseudo-

Cross-plots 1

R^2 factors	Atten. LWD Coaxial	Atten. Deep Coaxial	Atten. Deep Geosignal	Phase LWD Coaxial	Phase Deep Coaxial	Phase Deep Geosignal
Example B.1 Training	0.9997	0.9992	0.9509	0.9996	0.9994	0.9468
Test	0.9995	0.9984	0.9531	0.9990	0.9991	0.9487
Without Reg.						
Example B.1 Training	0.9998	0.9998	0.9897	0.9998	0.9998	0.9893
Test	0.9998	0.9998	0.9893	0.9998	0.9998	0.9890
With Reg.						
Example B.2 Training	0.9959	0.9975	0.9872	0.9954	0.9980	0.9853
Test	0.9924	0.9960	0.9775	0.9920	0.9974	0.9765
Without Reg.						

Cross-plots 2

R^2 factors	Atten. LWD Coaxial	Atten. Deep Coaxial	Atten. Deep Geosignal	Phase LWD Coaxial	Phase Deep Coaxial	Phase Deep Geosignal
Example B.1 Training	0.9997	0.9995	0.9998	0.9999	0.9996	0.9999
Test	0.9997	0.9994	0.9999	0.9999	0.9996	0.9999
Without Reg.						
Example B.1 Training	0.9971	0.9980	0.9779	0.9970	0.9979	0.9798
Test	0.9970	0.9979	0.9785	0.9970	0.9978	0.9803
With Reg.						
Example B.2 Training	0.9931	0.9958	0.9800	0.9933	0.9967	0.9821
Test	0.9890	0.9930	0.9701	0.9881	0.9944	0.9720
Without Reg.						

Table 2: R^2 factors for cross-plots 1 and 2 and Examples B.1 and B.2, with and without regularization, for training and test datasets. Numbers below 0.96 are marked in boldface.

inverse approximation encounters subsurface models for which the forward DNN approximation is untrained. As a result, both the forward and pseudo-inverse DDN approximations depart strongly from the true solutions, and they only comply with the only condition that their composition is close to the identity, which is insufficient to guarantee accurate approximations.

To partially alleviate the above problem, we envision three possible solutions. First, to increase the training dataset. This option is time-consuming and often impossible to achieve in practice. Notice we are already employing 1,000,000 samples. Second, to consider regularization. Results with regularization are

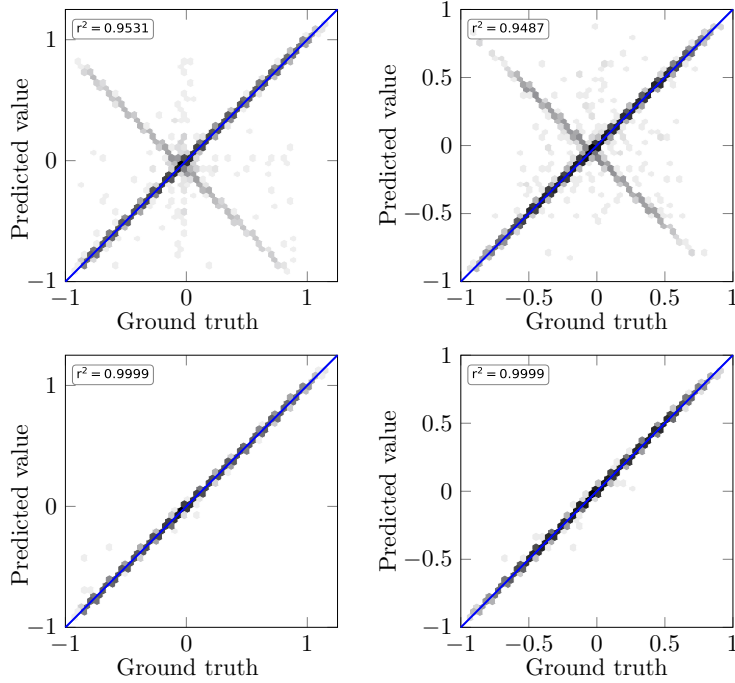


Figure 11: Geosignal cross plots for the Example B.1 without regularization for the test dataset. First row: Cross-plots 1. Second row: Cross-plots 2. First column: Attenuation. Second column: Phase.

Cross-plots 3

R^2 factors	Atten. LWD Coaxial	Atten. Deep Coaxial	Atten. Deep Geosignal	Phase LWD Coaxial	Phase Deep Coaxial	Phase Deep Geosignal
Example B.1 Without Reg.	0.9468	0.7406	0.0013	0.9383	0.9116	0.0167
With Reg.	0.9971	0.9979	0.9807	0.9969	0.9979	0.9856
Example B.2 Without Reg.	0.5721	0.8383	0.0253	0.4546	0.8611	0.0284
With Reg.	0.9010	0.9701	0.5901	0.8621	0.9618	0.5877

Table 3: R^2 factors for Cross-plots 3 and Examples B.1 and B.2, with and without regularization, for the test dataset.

of high quality (see Table 3). However, the regularization term may hide the presence of some physical solutions of the inverse problem, thus, diminishing the ability to perform uncertainty quantification and providing excessive confidence on the results. A third option is to consider the two-step loss function given by Equation 17. Following this approach, the forward DNN approximation is fixed before training the DNN pseudo-inverse approximation. This often

provides a proper DNN forward approximation even in areas with a lower rate of training samples before producing a DNN approximation that approximates the inverse of the DNN forward approximation. Following this two-step approach without regularization, we obtain high R^2 factors for cross-plots of type 3: above 0.95 for the geosignal attenuation and phase, and above 0.99 for the remaining measurements.

Finally, R^2 factors delivered by cross-plots of type 4 do not reflect on the accuracy of the DNN algorithm, but rather on the nature of the inverse problem at hand. If the R^2 factor is low, it indicates there exist multiple solutions. A simple way to increase the R^2 indicator is by incorporating regularization terms, like the one given by Equation 14. Figure 12 clearly illustrates this. However, it is misleading to conclude that results without regularization are worse. They are simply a different (but still valid) solution of the inverse problem.

8.3. Inversion of realistic synthetic models

To assess the performance of the inversion results, we consider three realistic synthetic examples. In terms of log accuracy, we observe qualitatively similar results for the attenuation and phase logs. Thus, for brevity of the exposition, in the following we display only the attenuation logs and omit the phase logs.

8.3.1. Model Problem I

Figure 13 describes a well trajectory in a synthetic model problem. The model is composed of a resistive layer with a water-bearing layer underneath, and it exhibits two geological faults.

For the DNNs produced with the Example B.2 (with input measurements corresponding to 65 logging positions per sample), Figure 14 shows the corresponding inverted models using the Encoder-Decoder DNN with and without regularization. Results show inaccurate inversion results, specially for the case without regularization. Moreover, predicted logs are distant from the true logs, as shown in Figure 15, and as expected from cross-plots 3 (see Table 3). Notice that DNN inversion results are *piecewise* 1D models. However, the DNN approximation is only trained for 1D models, not for piecewise 1D models, which explains the poor approximations we observe (see Remark A on Section 6).

In the remainder of this section, we restrict to DNNs produced with Example B.1. Figure 16 shows the corresponding inverted models. For the case of the encoder-decoder loss function without regularization, we observe in Figure 16a an inverted model that is completely different from the original one. The corresponding logs (see Figure 17) are also inaccurate, as anticipated by the cross-plots results of type 3 shown in the previous subsection. When considering the two-step loss function without regularization, the recovered model (see Figure 16b) is still quite different from the original one. Nonetheless, we observe a superb matching in the logs (see Figure 18), which indicates the presence of a different solution of the inverse problem. This confirms that the given measurements are insufficient to provide a unique solution for the inverse problem. For the case with regularization, inversion results (see Figure 16b) match the

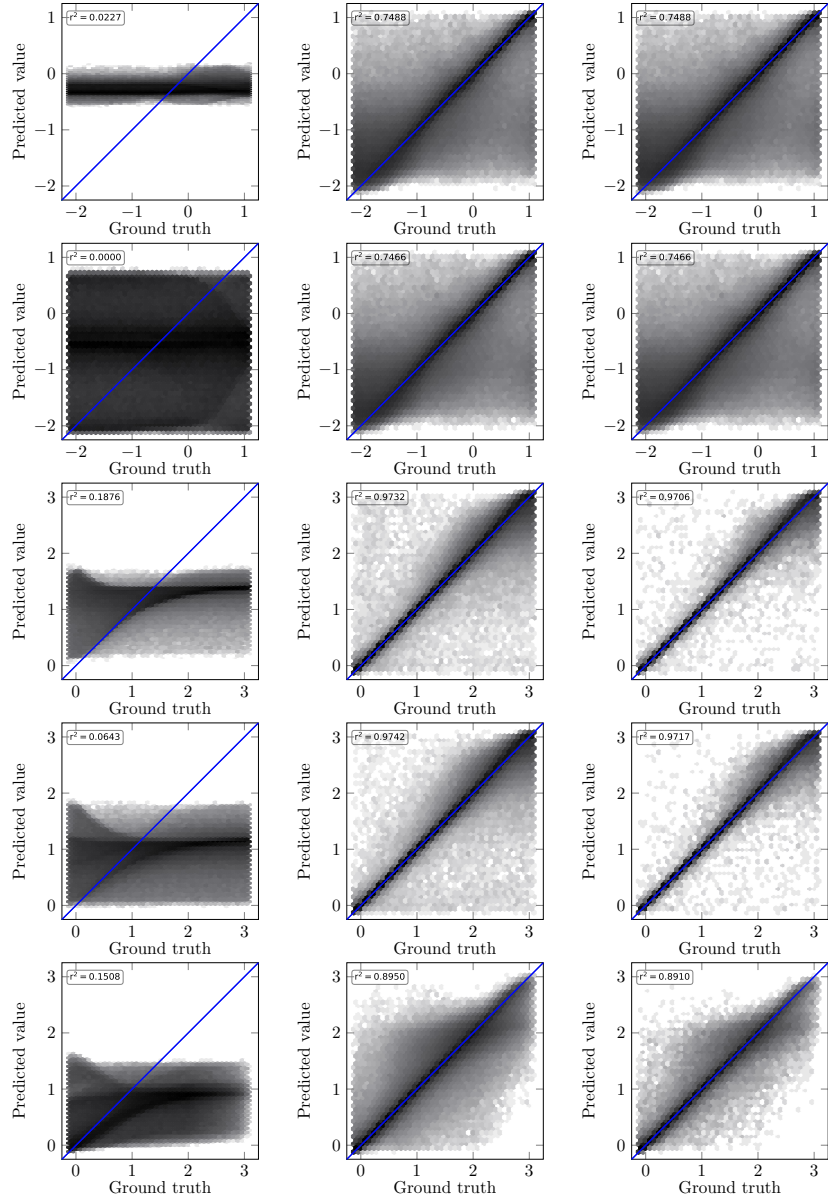


Figure 12: Cross-plots of type 4 for Example B.1 without regularization for the training dataset (first column), and with regularization for the training dataset (second column) and the test dataset (third column). First row: distance to the upper layer. Second row: distance to the lower layer. Third row: resistivity of upper layer. Fourth row: resistivity of lower layer. Fifth row: resistivity of central layer.

original model, and the corresponding logs properly approximate the synthetic ones, see Figures 19. Figures 20 and 21 confirm a proper training of the forward

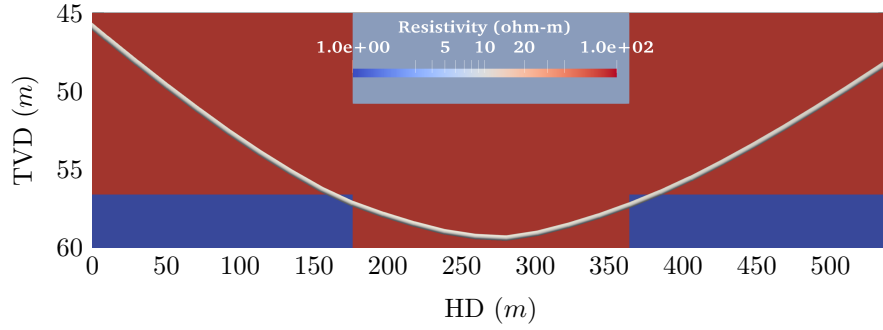
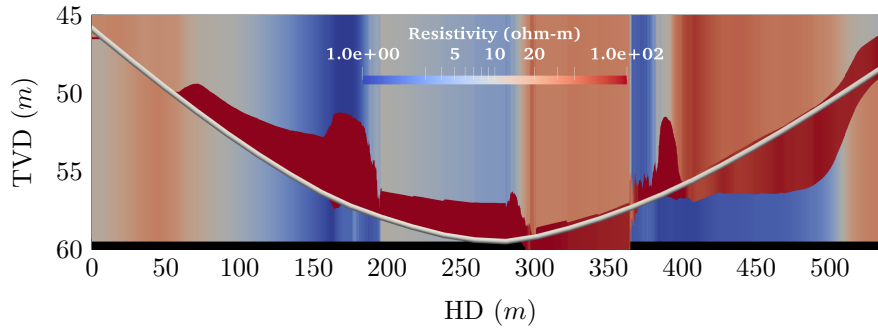
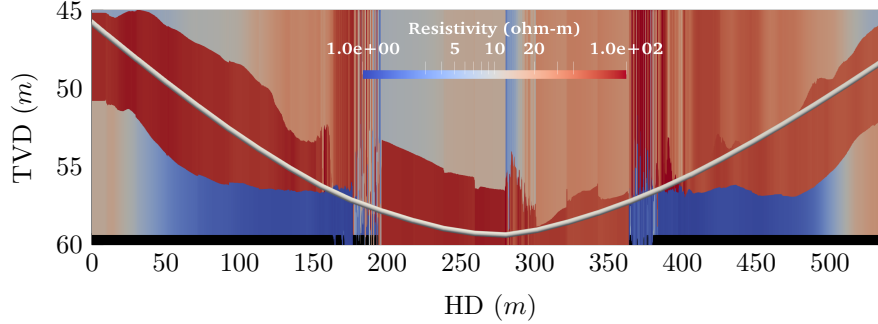


Figure 13: Formation of model problem I.



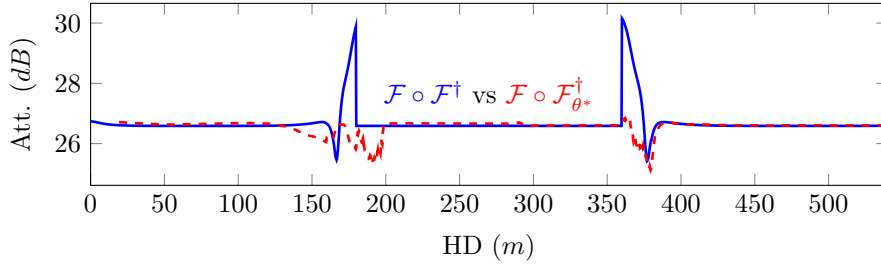
(a) Without regularization



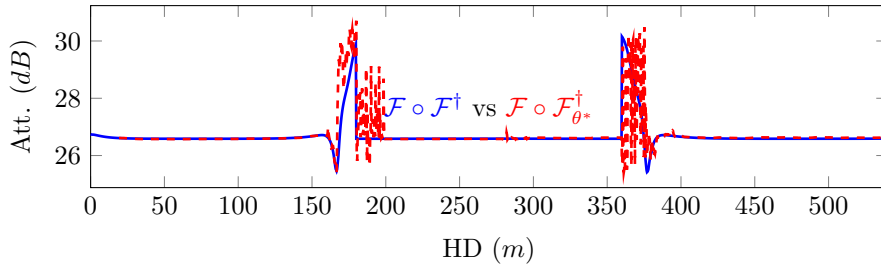
(b) With regularization

Figure 14: Inverted formation of model problem I using the inversion strategy of Example B.2, i.e., with input measurements corresponding to 65 logging positions per sample.

function approximation and the composition $\mathcal{F}_{\phi^*} \circ \mathcal{F}_{\theta^*}^\dagger$, respectively.



(a) LWD coaxial measurement. Without regularization



(b) LWD coaxial measurement. With regularization

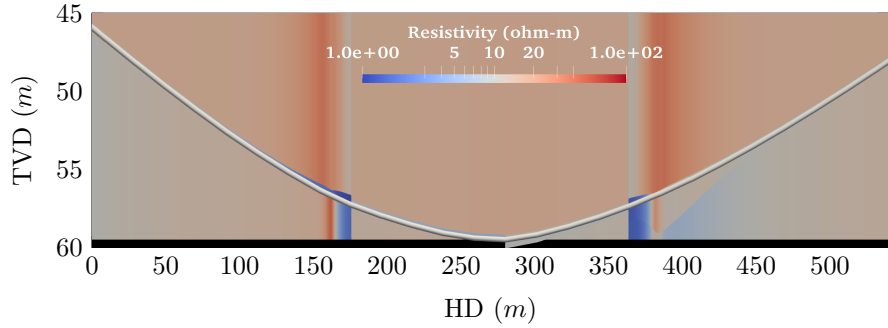
Figure 15: Model problem I. Comparison between $\mathcal{F} \circ \mathcal{F}^\dagger$ and $\mathcal{F} \circ \mathcal{F}_{\theta^*}^\dagger$ using the inversion strategy of Example B.2, i.e., with input measurements corresponding to 65 logging positions per sample.

8.3.2. Model Problem II

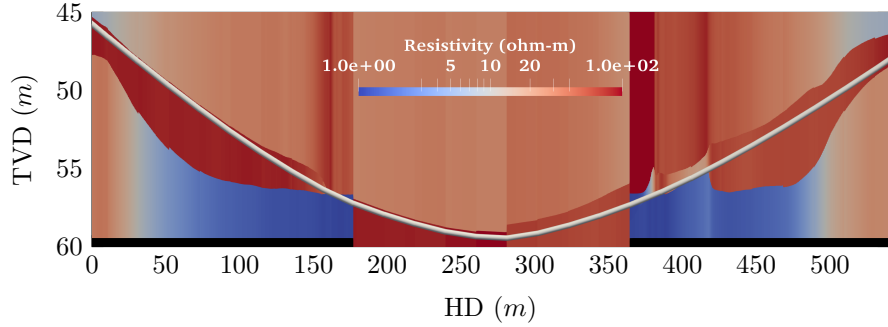
In this problem, we consider a 2.5m-thick conductive layer surrounded by two resistive layers. A well trajectory with a dip angle equal to 87° crosses the formation. Figure 22 displays the original and predicted models produced with DL. This example illustrates some of the limitations of DNNs. In here, earth models associated with part of the trajectory are outside the model problems considered in Section 2, which restrict to only one layer above and below the logging trajectory. Thus, the DNN is untrained for such models, and results cannot be trusted in those zones. Numerical results confirm these observations. Nonetheless, inaccurate inversion results are simple to identify by inspection of the logs (Figures 23 and 24).

8.3.3. Model Problem III

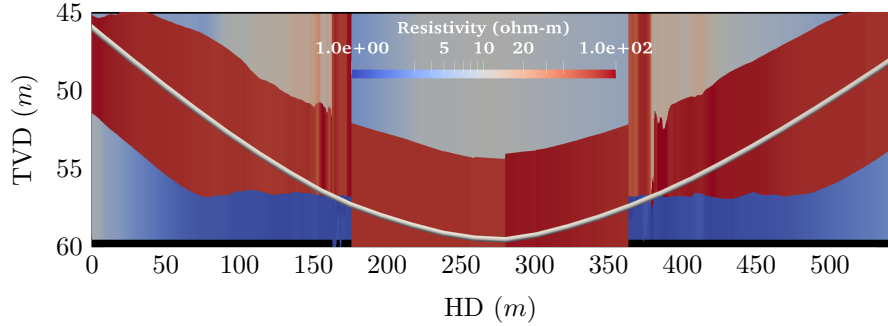
We now consider a model formation exhibiting geological faults and two different well trajectories. For well trajectory 1, Figure 25 shows the model problem, logging trajectory, inversion results, and coaxial attenuation logs. Inversion results are excellent. When considering the second well trajectory shown in Figure 26, we observe good inversion results except at the proximity of points with horizontal distance (HD) equals to 75m and 350m. These inaccurate inversion results are easily identified by examination of the corresponding logs.



(a) Predicted formation using the encoder-decoder loss function without regularization



(b) Predicted formation using the two-step loss function without regularization



(c) Predicted formation using the encoder-decoder loss function with regularization

Figure 16: Inverted formation of model problem I using the inversion strategy of Example B.1, i.e., with input measurements corresponding to one logging positions per sample.

9. Discussion and conclusions

In this work, we have focused on the DNN inversion of borehole resistivity measurements with geosteering applications. First, we have analyzed the

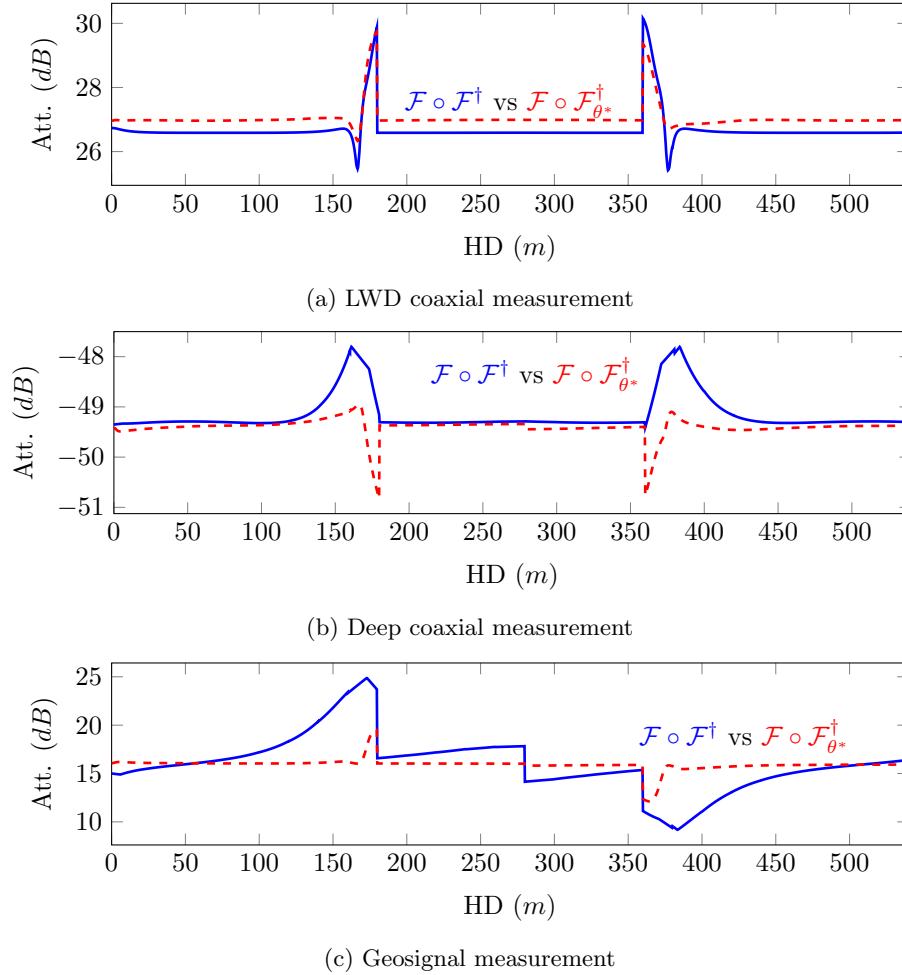
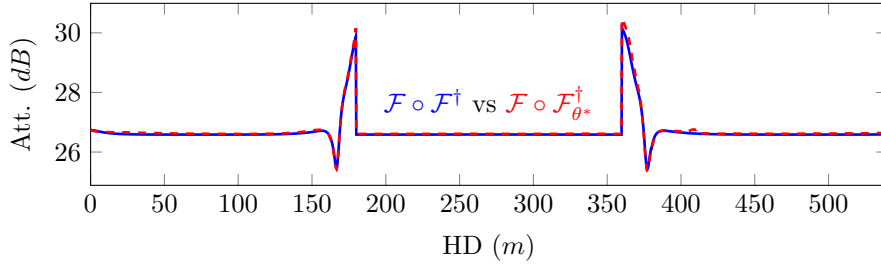


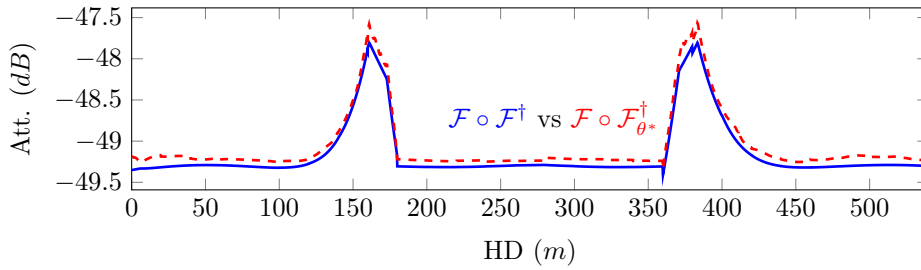
Figure 17: Model problem I. Comparison between $\mathcal{F} \circ \mathcal{F}^\dagger$ and $\mathcal{F} \circ \mathcal{F}_{\theta^*}^\dagger$ without regularization using the encoder-decoder loss function and the inversion strategy of Example B.1, i.e., with input measurements corresponding to one logging positions per sample.

strong impact that the use of different loss functions have on the results. We illustrate via a simple benchmark example that a traditional data misfit loss function delivers poor results. As a remedy to that, we propose the use of an encoder-decoder or a two-step loss function. These approaches generate two DNN approximations: one for the forward function and another one for the inverse operator. Different architectures should be used to approximate these functions via DNNs.

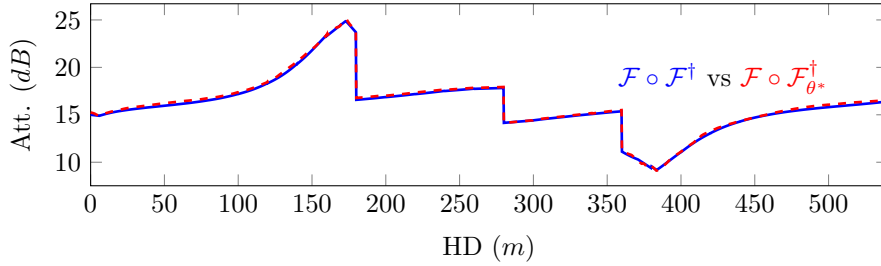
To guarantee that the inverse DNN approximation provides meaningful results, we need to ensure that the training dataset contains sufficient samples. Otherwise, both forward and inverse DNN operators may provide incorrect so-



(a) LWD coaxial measurement



(b) Deep coaxial measurement



(c) Geosignal measurement

Figure 18: Model problem I. Comparison between $\mathcal{F} \circ \mathcal{F}^\dagger$ and $\mathcal{F} \circ \mathcal{F}_{\theta^*}^\dagger$ using the two-step loss function without regularization and the inversion strategy of Example B.1, i.e., with input measurements corresponding to one logging positions per sample.

lutions while still ensuring the composition of both operators to be close to the identity. Thus, the approach is highly dependent on the existence of a sufficiently rich training dataset, which facilitates the learning process of the DNNs. In the case of 1D layered formations, it is often feasible to produce the required dataset. However, for more complicated cases, e.g., 2D and 3D inversions, a direct extension may be limited due to the larger number of inversion variables and the time-consuming process of dataset production.

As a partial remedy for this limitation, we encounter highly beneficial to add a regularization term to the loss function based on the existing training dataset.

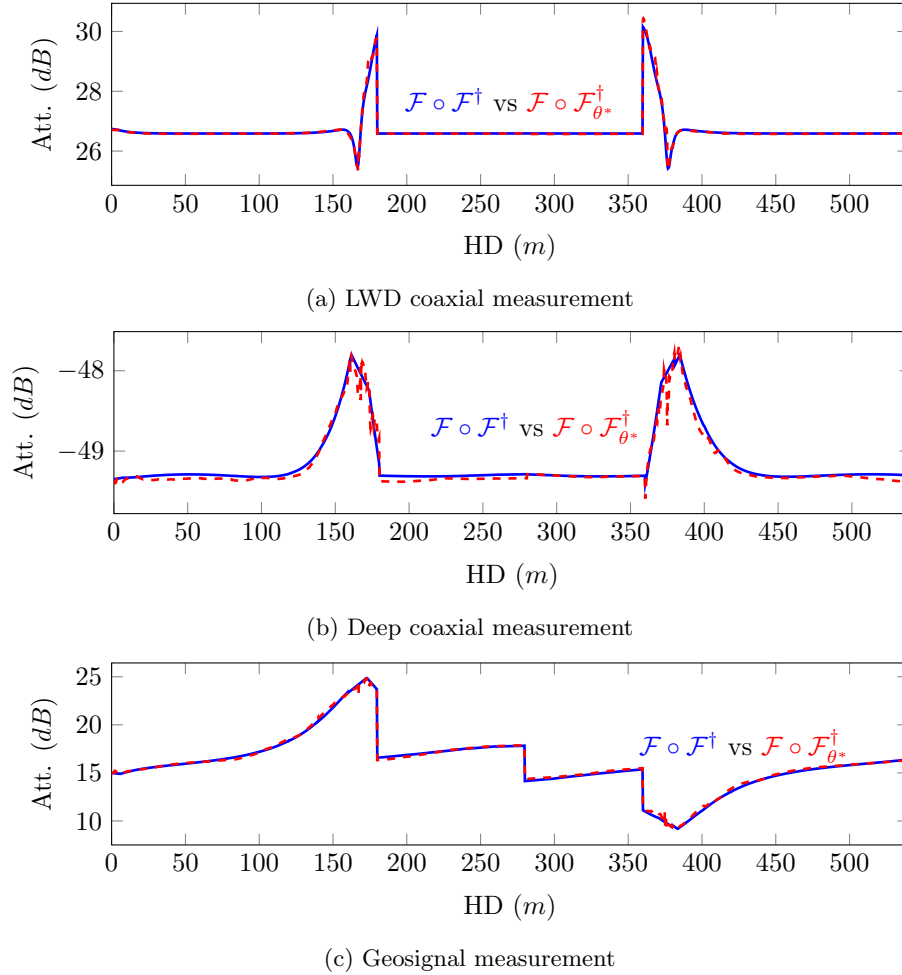


Figure 19: Model problem I. Comparison between $\mathcal{F} \circ \mathcal{F}^\dagger$ and $\mathcal{F} \circ \mathcal{F}_{\theta^*}^\dagger$ with regularization using the inversion strategy of Example B.1, i.e., with input measurements corresponding to one logging positions per sample.

This reduces the needed richness of the training datasets. On the other side, such regularization term hides other possibly existing solutions for the inverse operator, which may provide excessive confidence on the results and minimize the capacity to perform a fair uncertainty quantification assessment. Another possibility to partially alleviate the aforementioned problem is to consider a two-step loss functions. Using this approach, we have shown that the inverse problem considered in this work admits different solutions that are physically feasible, a fact that was unnoticed when using the regularization term.

Other critical limitations about DNNs we encountered in this work are: (a) the limited approximation capabilities of DNNs to reproduce discontinuous

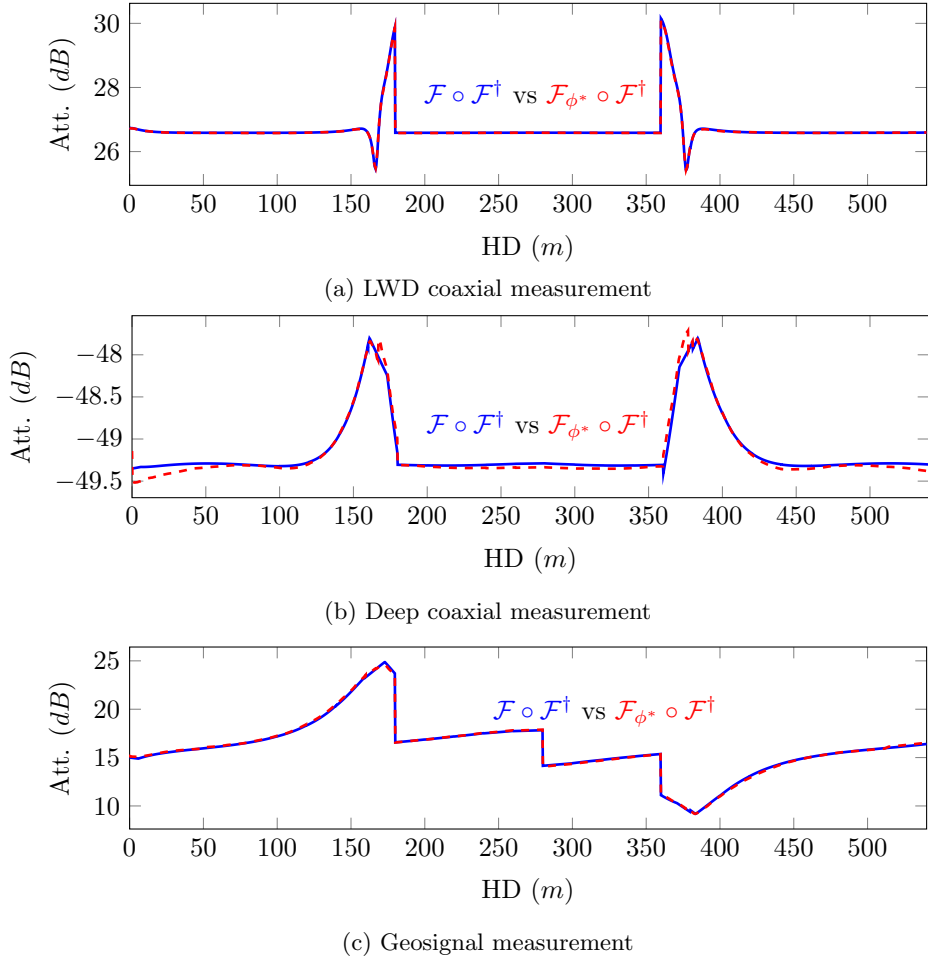


Figure 20: Model problem I. Comparison between $\mathcal{F} \circ \mathcal{F}^\dagger$ and $\mathcal{F}_{\phi^*} \circ \mathcal{F}^\dagger$ with regularization using the inversion strategy of Example B.1, i.e., with input measurements corresponding to one logging positions per sample.

functions, (b) the need of a new dataset and trained DNN for each subsurface parametrization, and (c) the poor results they exhibit when they are evaluated over a sample that is outside the training dataset space. More importantly, it is often difficult to identify the source of poor results, which may include inadequate selections of: (i) loss function, (ii) DNN architecture, (iii) regularization term, (iv) training dataset, (v) optimization algorithm, (vi) rescaling operator and norms, (vii) model parameterization, (viii) approximation capabilities of DNNs, or simply (ix) the nature of the problem due to a lack of adequate measurements. To deal with the aforementioned limitations, we propose a careful step-by-step error control based on: (a) selecting adequate norms, (b) properly rescaling the variables, (c) selecting a well suited loss function possibly with a

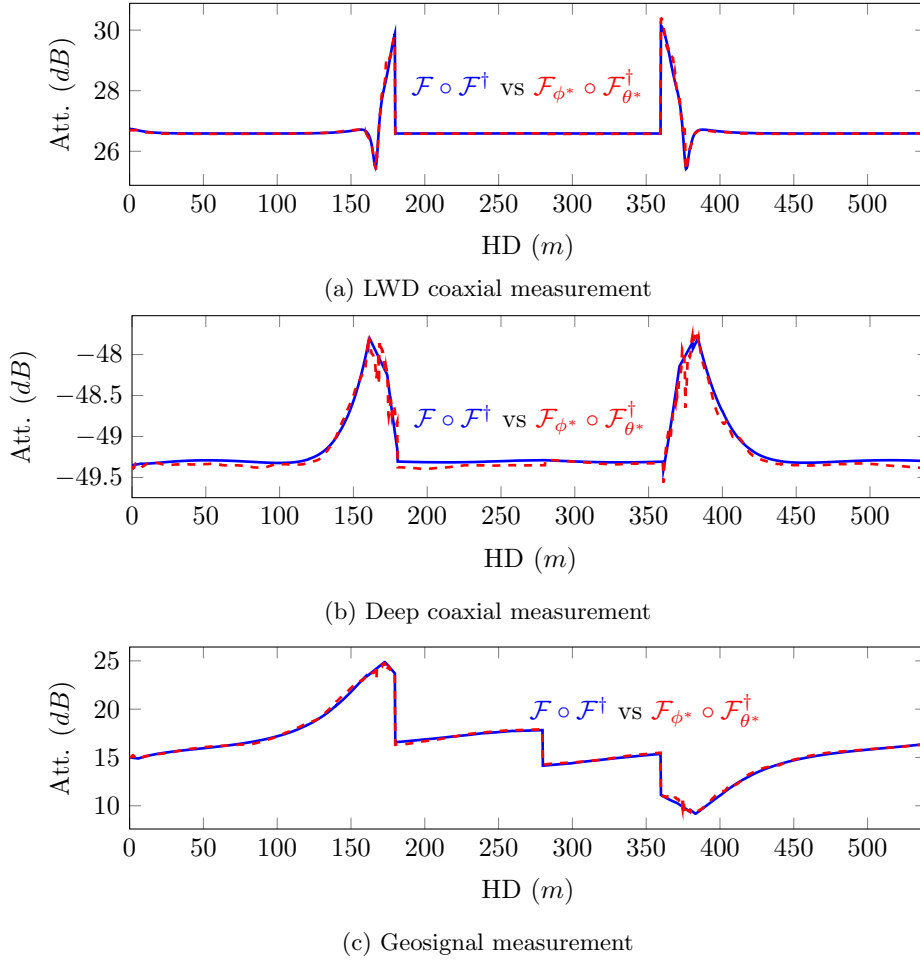
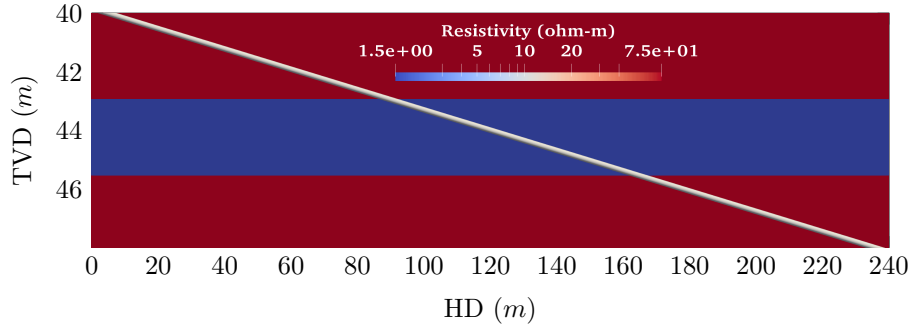


Figure 21: Model problem I. Comparison between $\mathcal{F} \circ \mathcal{F}^\dagger$ and $\mathcal{F}_{\phi^*} \circ \mathcal{F}_{\theta^*}^\dagger$ with regularization using the inversion strategy of Example B.1, i.e., with input measurements corresponding to one logging positions per sample.

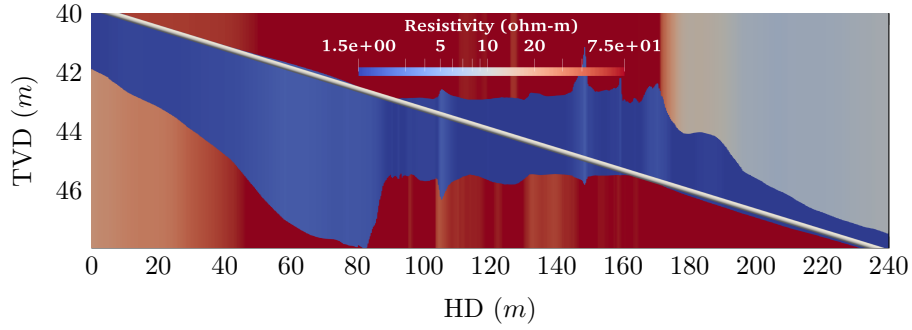
regularization term, (d) analyzing the evolution of the different terms of the loss function, (e) studying multiple cross-plots of different nature, and (f) performing an in-depth assessment of the results over multiple realistic test examples.

Finally, we showed it is possible to obtain a good-quality inversion of geosteering measurements with limited *online* computational cost, thus, suitable for real-time inversion. Moreover, the quality of the inversion results can be rapidly evaluated to detect its possible inaccuracies in the field and select alternative inversion methods when needed.

Possible continuation research lines of this work include: (a) to study different DNN architectures when applied to these problems, for example, using automatic DNN architecture generators such as AutoML techniques, (b) to



(a) Actual formation



(b) Predicted formation using one logging position with regularization

Figure 22: Model problem 2. Comparison between actual and predicted formations with regularization using the inversion strategy of Example B.1, i.e., with input measurements corresponding to one logging positions per sample.

design proper measurement acquisition systems and adequate earth model parameterisations using the cross-plots delivered by the DNNs, (c) to consider more complex Earth models, possibly containing geological faults or other relevant subsurface features, (d) to develop optimal sampling techniques for inverse problems, possibly containing a different number of samples to train the forward and inverse operators, (e) to design and analyse new regularization techniques, (f) to use Bayesian DNNs for uncertainty quantification, and (g) to use transfer learning techniques for higher spatial dimensions, which can alleviate data requirements to train the corresponding DNNs. In the end, a natural step toward industrial applications is to evaluate the performance of our DNN approach when having noisy measurements. As mentioned above, we shall use our approach to design proper measurement acquisition techniques and adequate earth model parameterizations using the cross-plots delivered by the DNNs.

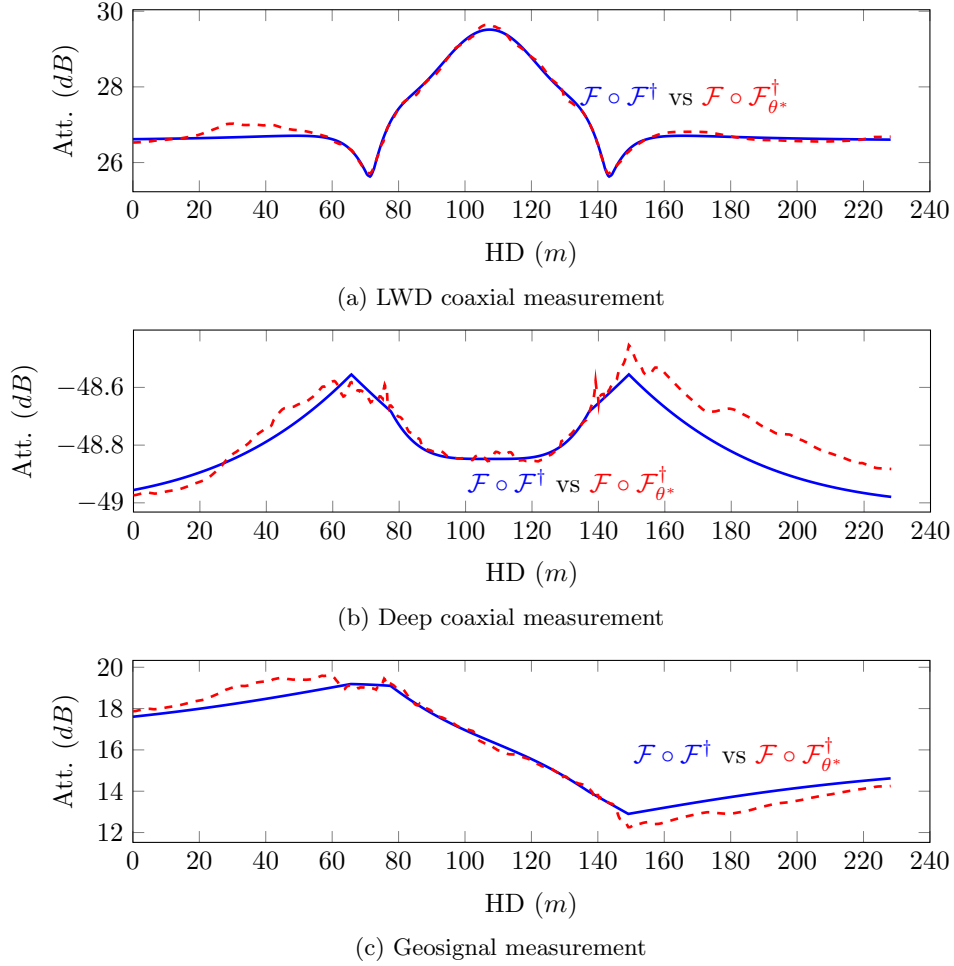


Figure 23: Model problem 2. Comparison between $\mathcal{F} \circ \mathcal{F}^\dagger$ and $\mathcal{F} \circ \mathcal{F}_{\theta^*}^\dagger$ with regularization using the inversion strategy of Example B.1, i.e., with input measurements corresponding to one logging positions per sample.

10. Acknowledgments

The research reported in this article has been funded by the European Union's Horizon 2020 research and innovation programme under the Marie Skłodowska-Curie grant agreement No 777778 (MATHROCKS), the Austrian Ministry for Transport, Innovation and Technology (BMVIT), the Federal Ministry for Digital and Economic Affairs (BMDW), the Province of Upper Austria in the frame of the COMET - Competence Centers for Excellent Technologies Program managed by Austrian Research Promotion Agency FFG, the Project of the Spanish Ministry of Economy and Competitiveness with reference

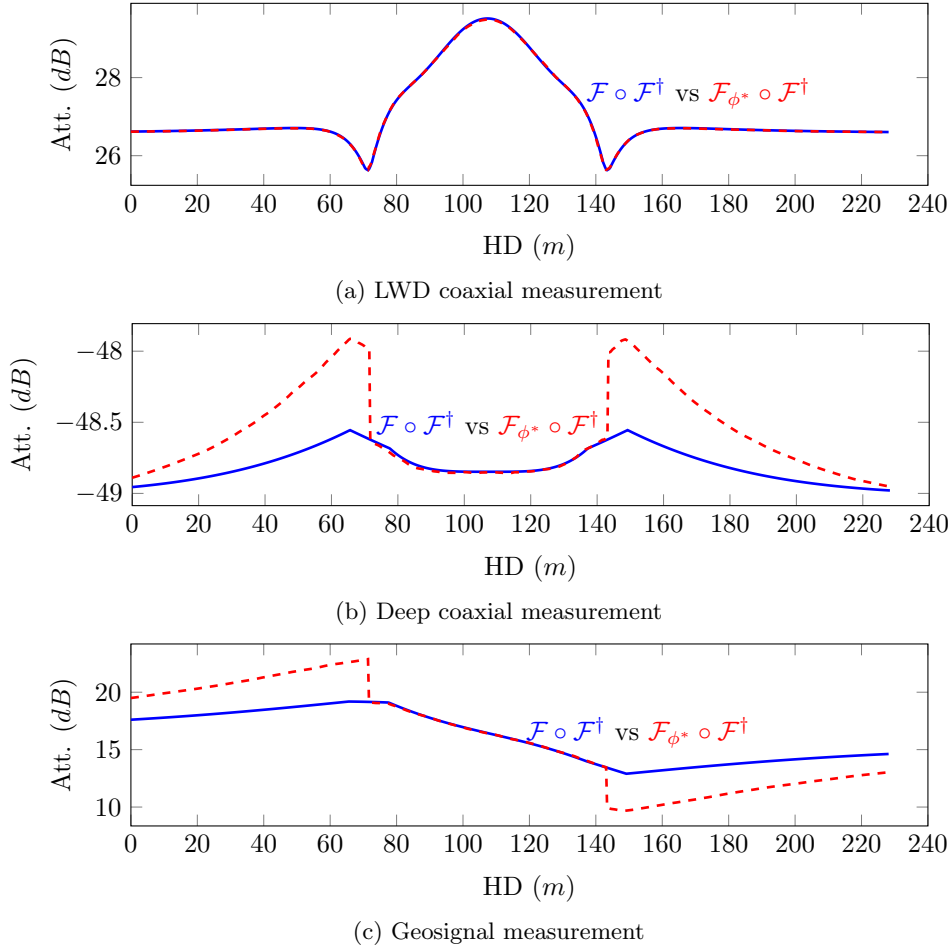
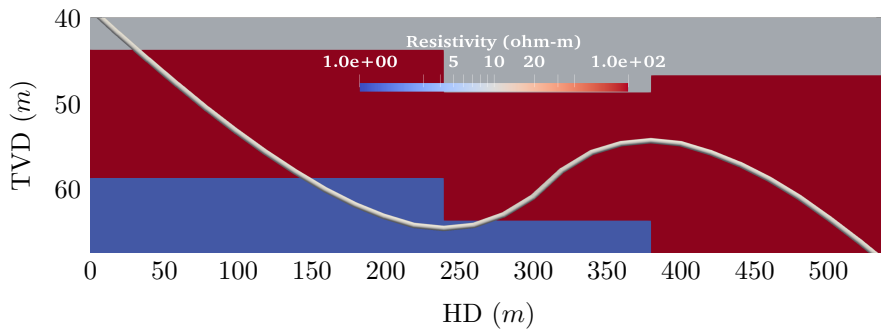
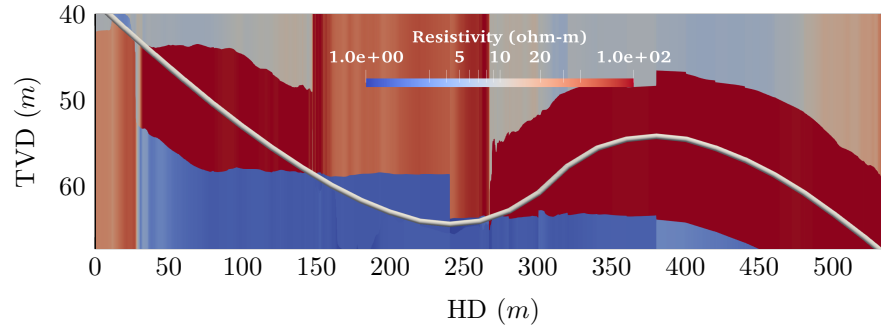


Figure 24: Model problem 2. Comparison between $\mathcal{F} \circ \mathcal{F}^\dagger$ and $\mathcal{F}_{\phi^*} \circ \mathcal{F}^\dagger$ with regularization using the inversion strategy of Example B.1, i.e., with input measurements corresponding to one logging positions per sample.

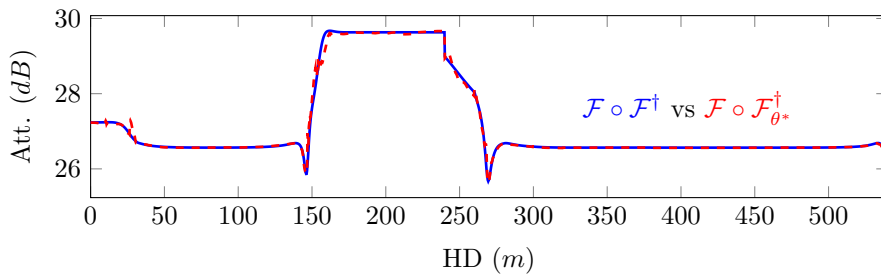
MTM2016-76329-R (AEI/FEDER, EU), the BCAM “Severo Ochoa” accreditation of excellence (SEV-2017-0718), and the Basque Government through the BERC 2018-2021 program, the two Elkartek projects ArgIA (KK-2019-00068) and MATHEO (KK-2019-00085), the Consolidated Research Group MATH-MODE (IT1294-19) given by the Department of Education, The University of Texas at Austin Research Consortium on Formation Evaluation, jointly sponsored by Anadarko, Aramco, Baker Hughes, BHP, BP, Chevron, China Oilfield Services Limited, CNOOC International, ConocoPhillips, DEA, Eni, Equinor ASA, ExxonMobil, Halliburton, INPEX, Lundin Norway, Occidental, Oil Search, Petrobras, Repsol, Schlumberger, Shell, Southwestern, Total, Wintershall Dea, and Woodside Petroleum Limited. Carlos Torres-Verdín is grateful for the finan-



(a) Actual formation



(b) Predicted formation



(c) LWD coaxial measurement

Figure 25: Model problem III, trajectory 1. Comparison between actual and predicted formations and the corresponding coaxial logs with regularization using the inversion strategy of Example B.1, i.e., with input measurements corresponding to one logging positions per sample.

cial support provided by the Brian James Jennings Memorial Endowed Chair in Petroleum and Geosystems Engineering.

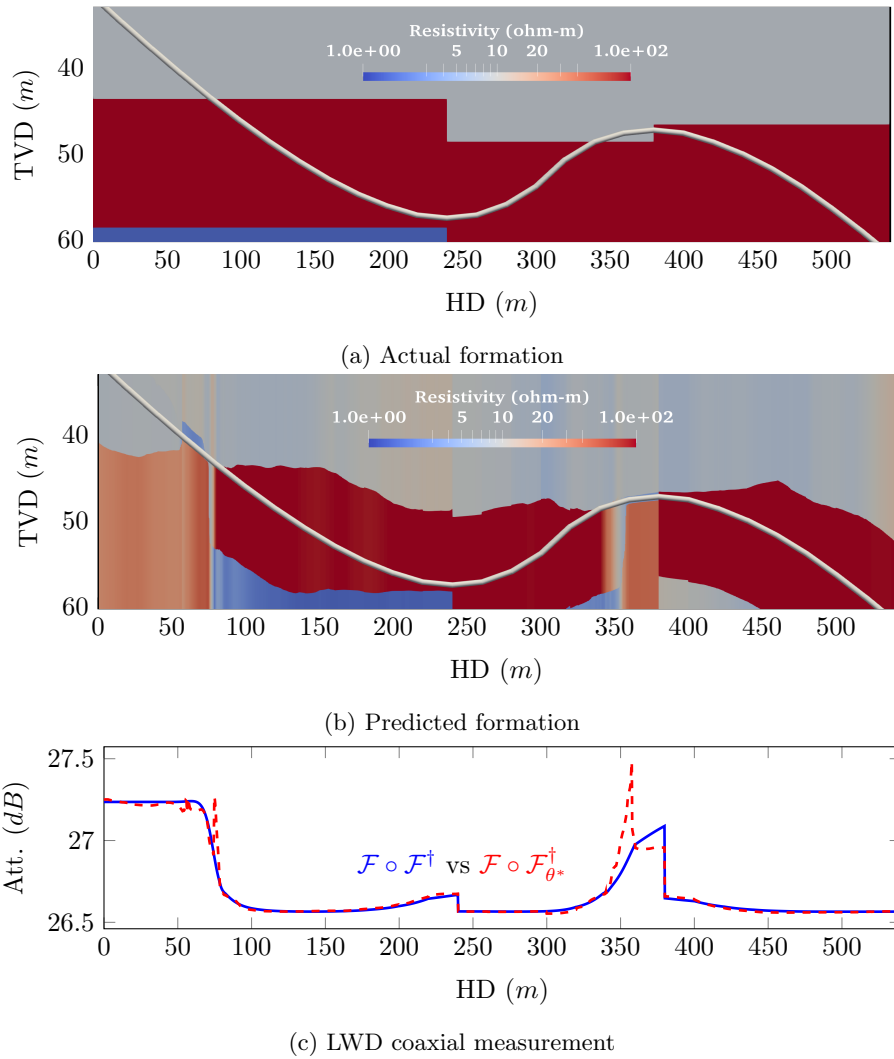


Figure 26: Model problem III, Trajectory 2. Comparison between actual and predicted formations and the corresponding coaxial logs with regularization using the inversion strategy of Example B.1, i.e., with input measurements corresponding to one logging positions per sample.

References

- [1] L. Lu, Y. Zheng, G. Carneiro, L. Yang, Deep Learning for Computer Vision: Expert techniques to train advanced neural networks using TensorFlow and Keras, Springer, Switzerland, 2017.
- [2] D. Yu, L. Deng, Automatic Speech Recognition: A Deep Learning approach, Springer, London, 2017.

- [3] B. Bhanu, A. Kumar, *Deep Learning for Biometrics*, Springer, Switzerland, 2017.
- [4] K. He, X. Zhang, S. Ren, J. Sun, Deep residual learning for image recognition, arXiv:1512.03385 (2015).
- [5] V. Badrinarayanan, A. Kendall, R. Cipolla, Segnet: A deep convolutional encoder-decoder architecture for image segmentation, *IEEE Transactions on Pattern Analysis and Machine Intelligence* 39 (12) (2017) 2481–2495.
- [6] F. Chollet, Keras, <https://github.com/fchollet/keras> (2015).
- [7] A. Paszke, S. Gross, S. Chintala, G. Chanan, E. Yang, Z. DeVito, Z. Lin, A. Desmaison, L. Antiga, A. Lerer, Automatic differentiation in pytorch, in: *NIPS-W*, 2017.
- [8] R. Zhao, R. Yan, Z. Chen, K. Mao, P. Wang, R. X. Gao, Deep learning and its applications to machine health monitoring, *Mechanical Systems and Signal Processing* 115 (2019) 213 – 237. doi:<https://doi.org/10.1016/j.ymsp.2018.05.050>.
- [9] L. Deng, J. Li, J. Huang, K. Yao, D. Yu, F. Seide, M. Seltzer, G. Zweig, X. He, J. Williams, Y. Gong, A. Acero, Recent advances in deep learning for speech research at microsoft, in: *2013 IEEE International Conference on Acoustics, Speech and Signal Processing*, 2013, pp. 8604–8608.
- [10] M. Lngkvist, L. Karlsson, A. Loutfi, A review of unsupervised feature learning and deep learning for time-series modeling, *Pattern Recognition Letters* 42 (2014) 11 – 24. doi:<https://doi.org/10.1016/j.patrec.2014.01.008>.
- [11] R. Vargas, A. Mosavi, R. Ruiz, Deep learning: A review, Working paper (January 2017).
- [12] B. Jan, H. Farman, M. Khan, M. Imran, I. U. Islam, A. Ahmad, S. Ali, G. Jeon, Deep learning in big data analytics: A comparative study, *Computers & Electrical Engineering* 75 (2019) 275 – 287. doi:<https://doi.org/10.1016/j.compeleceng.2017.12.009>.
- [13] M. Shahriari, D. Pardo, A. Picón, A. Galdran, J. D. Ser, C. Torres-Verdín, A deep learning approach to the inversion of borehole resistivity measurements, *Computational Geosciences* (2020). doi:[10.1007/s10596-019-09859-y](https://doi.org/10.1007/s10596-019-09859-y).
- [14] D. Pardo, C. Torres-Verdin, Fast 1D inversion of logging-while-drilling resistivity measurements for the improved estimation of formation resistivity in high-angle and horizontal wells, *Geophysics* 80 (2) (2014) E111–E124.
- [15] O. Ijasana, C. Torres-Verdín, W. E. Preeg, Inversion-based petrophysical interpretation of logging-while-drilling nuclear and resistivity measurements, *Geophysics* 78 (6) (2013) D473–D489.

- [16] R. Desbrandes, R. Clayton, Chapter 9 measurement while drilling, *Developments in Petroleum Science* 38 (1994) 251 – 279.
- [17] M. Ghasemi, Y. Yang, E. Gildin, Y. Efendiev, V. M. Calo, Fast multiscale reservoir simulations using pod-deim model reduction, *Society of Petroleum Engineers* (2015) 1–18.
- [18] R. Chemali, M. Bittar, F. Hveding, M. Wu, M. Dautel, Improved geosteering by integrating in real time images from multiple depths of investigation and inversion of azimuthal resistivity signals, *Society of Petrophysicists and Well-Log Analysts* (2010) 1–7.
- [19] C. Dupuis, J. M. Denichou, Automatic inversion of deep-directional-resistivity measurements for well placement and reservoir description, *The Leading Edge* 34 (5) (2015) 504–512.
- [20] Z. Zhang, N. Yuan, C. R. Liu, 1-D inversion of triaxial induction logging in layered anisotropic formation, *Progress In Electromagnetics Research B* 44 (2012) 383–403.
- [21] D. J. Seifert, S. A. Dossary, R. E. Chemali, M. S. Bittar, A. A. Lotfy, J. L. Pitcher, M. A. Bayrakdar, Deep electrical images, geosignal, and real-time inversion help guide steering decisions, *Society of Petroleum Engineers* (2009) 1–9.
- [22] A. Tarantola, *Inverse Problem Theory and Methods for Model Parameter Estimation*, Society for Industrial and Applied Mathematics, 2005.
- [23] M. Shahriari, S. Rojas, D. Pardo, A. Rodríguez-Rozas, S. A. Bakr, V. M. Calo, I. Muga, A numerical 1.5D method for the rapid simulation of geophysical resistivity measurements, *Geosciences* 8(6) (2018) 1–28.
- [24] L. Wang, H. Li, Y. Fan, Bayesian inversion of logging-while-drilling extra-deep directional resistivity measurements using parallel tempering markov chain monte carlo sampling, *IEEE Transactions on Geoscience and Remote Sensing* 57 (10) (2019) 8026–8036.
- [25] A. Malinverno, C. Torres-Verdín, Bayesian inversion of DC electrical measurements with uncertainties for reservoir monitoring, *Inverse Problems* 16 (5) (2000) 1343–1356. doi:10.1088/0266-5611/16/5/313.
- [26] J. Gunning, M. E. Glinsky, Detection of reservoir quality using bayesian seismic inversion, *GEOPHYSICS* 72 (3) (2007) R37–R49. doi:10.1190/1.2713043.
- [27] C. Vogel, *Computational Methods for Inverse Problems*, Society for Industrial and Applied Mathematics, 2002.
- [28] C. F. Higham, D. J. Higham, Deep learning: An introduction for applied mathematicians, *Computing Research Repository* abs/1801.05894 (2018).

- [29] M. Shahriari, D. Pardo, B. Moser, F. Sobieczky, A deep neural network as surrogate model for forward simulation of borehole resistivity measurements, *Procedia Manufacturing* 42 (2020) 235 – 238, international Conference on Industry 4.0 and Smart Manufacturing (ISM 2019).
- [30] J. Alvarez-Aramberri, D. Pardo, Dimensionally adaptive hp-finite element simulation and inversion of 2D magnetotelluric measurements, *Journal of Computational Science* 18 (2017) 95–105.
- [31] S. A. Bakr, D. Pardo, T. Mannseth, Domain decomposition Fourier FE method for the simulation of 3D marine CSEM measurements, *J. Comput. Phys.* 255 (2013) 456–470.
- [32] S. Davydycheva, T. Wang, A fast modelling method to solve Maxwell’s equations in 1D layered biaxial anisotropic medium, *Geophysics* 76 (5) (2011) F293–F302.
- [33] S. Davydycheva, D. Homan, G. Minerbo, Triaxial induction tool with electrode sleeve: FD modeling in 3D geometries, *Journal of Applied Geophysics* 67 (2004) 98–108.
- [34] L. O. Loseth, B. Ursin, Electromagnetic fields in planarly layered anisotropic media, *Geophysical Journal International* 170 (2007) 44–80.
- [35] A. Rahimpour, A. Taalimi, H. Qi, Feature encoding in band-limited distributed surveillance systems, in: 2017 IEEE International Conference on Acoustics, Speech and Signal Processing (ICASSP), IEEE, 2017, pp. 1752–1756.
- [36] Y. Jin, X. Wu, J. Chen, Y. Huang, et al., Using a physics-driven deep neural network to solve inverse problems for lwd azimuthal resistivity measurements, in: SPWLA 60th Annual Logging Symposium, Society of Petrophysicists and Well-Log Analysts, 2019.
- [37] M. Abadi, A. Agarwal, P. Barham, E. Brevdo, Z. Chen, C. Citro, G. S. Corrado, A. Davis, J. Dean, M. Devin, S. Ghemawat, I. Goodfellow, A. Harp, G. Irving, M. Isard, Y. Jia, R. Jozefowicz, L. Kaiser, M. Kudlur, J. Levenberg, D. Mané, R. Monga, S. Moore, D. Murray, C. Olah, M. Schuster, J. Shlens, B. Steiner, I. Sutskever, K. Talwar, P. Tucker, V. Vanhoucke, V. Vasudevan, F. Viégas, O. Vinyals, P. Warden, M. Wattenberg, M. Wicke, Y. Yu, X. Zheng, TensorFlow: Large-scale machine learning on heterogeneous systems, software available from tensorflow.org (2015).
- [38] T. M. Quan, D. G. C. Hildebrand, W.-K. Jeong, Fusionnet: A deep fully residual convolutional neural network for image segmentation in connectomics (2016). [arXiv:1612.05360](https://arxiv.org/abs/1612.05360).
- [39] A. Krizhevsky, I. Sutskever, G. E. Hinton, Imagenet classification with deep convolutional neural networks, in: F. Pereira, C. J. C. Burges, L. Bottou,

K. Q. Weinberger (Eds.), *Advances in Neural Information Processing Systems 25*, Curran Associates, Inc., 2012, pp. 1097–1105.

- [40] K. H. Jin, M. T. McCann, E. Froustey, M. Unser, Deep convolutional neural network for inverse problems in imaging, *IEEE Transactions on Image Processing* 26 (9) (2017) 4509–4522.

Appendices

A. Measurements acquisition system

We first consider a co-axial LWD instrument equipped with two transmitters and two receivers (see Figure 27). H_{zz}^1 and H_{zz}^2 are the zz -couplings of the magnetic field measured at the first and the second receivers, respectively (the first and second subscripts denote the orientation of the transmitter and receiver, respectively). Then, we define the attenuation and phase difference as follows:

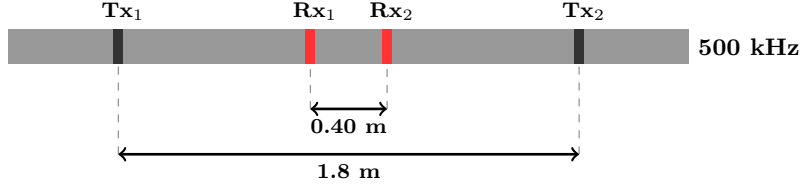


Figure 27: Conventional LWD logging instrument. Tx_i and Rx_i are the transmitters and the receivers, respectively.

$$\ln \frac{H_{zz}^1}{H_{zz}^2} = \underbrace{\ln \frac{|H_{zz}^1|}{|H_{zz}^2|}}_{\times 20 \log(e) =: \text{attenuation (dB)}} + i \underbrace{\left(\text{ph}(H_{zz}^1) - \text{ph}(H_{zz}^2) \right)}_{\times \frac{180}{\pi} =: \text{phase difference (degree)}}, \quad (20)$$

where ph denotes the phase of a complex number. We then record the average of the attenuations and phase differences associated with the two transmitters, and we denote these values as *LWD coaxial*.

Then, we consider a short-spacing configuration corresponding to a deep azimuthal instrument equipped with one transmitter and one receiver, as shown in Figure 28. In this logging instrument, the distance between transmitter and receiver is significantly larger than that of the previously considered LWD instrument. It also employs tilted receivers that are sensitive to the presence of bed boundaries. We record several measurements with this logging instrument: (a) the attenuation and phase differences, denotes as *deep coaxial*, computed

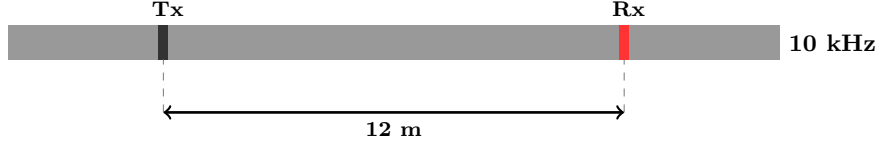


Figure 28: Short-spacing of a deep azimuthal logging instrument. Tx and Rx are the transmitter and the receiver, respectively.

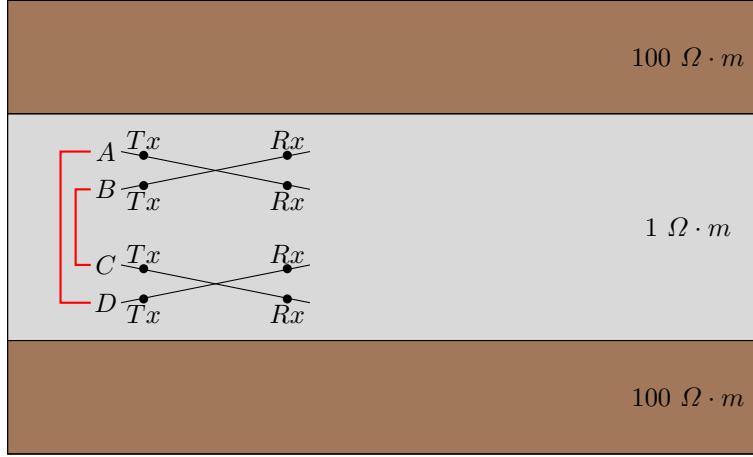


Figure 29: Illustration with four logging trajectories. By symmetry, measurements recorded with trajectories A and D are identical. The same occurs with trajectories B and C. If these measurements are continuous with respect to the dip angle, then at 90 degrees they all become identical, which disables the possibility of identifying if a nearby bed boundary is located on top or on the bottom of the logging instrument.

using Equation (20) with $H_{zz}^2 = 1$, and (b) the attenuation and phase differences of a directional measurement expressed as:

$$\begin{aligned}
 Geosignal = \ln \frac{H_{zz} - H_{zx}}{H_{zz} + H_{zx}} = & \underbrace{\ln \frac{|H_{zz} - H_{zx}|}{|H_{zz} + H_{zx}|}}_{\times 20 \log(e) =: \text{attenuation (dB)}} \\
 & + i \underbrace{(\text{ph}(H_{zz} - H_{zx}) - \text{ph}(H_{zz} + H_{zx}))}_{\times \frac{180}{\pi} =: \text{phase difference (degree)}}. \quad (21)
 \end{aligned}$$

We denote it as *geosignal*. These measurements exhibit a discontinuity as a function of the dip angle at 90 degrees. Indeed, such discontinuity is essential in the measurements if one wants to discern between top and bottom of the logging instrument—see Figure 29.

We consider two types of logging trajectories. In one case, corresponding to Example B.1, each trajectory consists of a single logging position, and the set of

measurements is given by 6 real numbers. For the Example B.2, each trajectory contains 65 logging positions with a logging step size of 0.3048 m . Thus, our set of measurements per logging trajectory consist of 195 pairs of real numbers (see [13, 29] for further details).

B. DDN Architectures

In this work, we use DNN architectures based on residual blocks [4, 38] with convolutional operators [28, 39, 40] to approximate the forward and the inverse problems.

B.1. Forward Problem DNN Architecture

We consider:

$$\mathcal{F}_{\mathcal{R},\phi} := \mathbf{I}_{\phi_N}^{c_1} \circ \mathcal{L} \circ \mathcal{B}_{\phi_{N-1}}^{N-1} \circ \mathcal{B}_{\phi_{N-2}}^{N-2} \circ \dots \circ \mathcal{B}_{\phi_1}^1, \quad (22)$$

where $\phi = \{\phi_i : i = 1, \dots, N\}$ is a set of all weights associated to each block and layer. In Equation (22), $\{\mathcal{B}_{\phi_i}^i : i = 1, \dots, 5\}$ consist of an upsampling layer followed by residual blocks. Specifically:

$$\mathcal{B}_{\phi_i}^i := \left(\mathcal{N} \circ \mathbf{I}_{\phi_i}^{c_i} \circ \mathcal{N} \circ \mathbf{I}_{\phi_i}^{c_i} + \mathcal{I} \right) \circ \mathcal{U}, \quad (23)$$

where \mathbf{I}_{ϕ}^c is a convolutional layer with c_i as its convolution window, \mathcal{I} is the identity function, \mathcal{U} is a one-dimensional upsampling that raises the dimension of the output of the residual block gradually to avoid missing information due to a sudden expansion of dimension, $\mathbf{I}_{\phi_N}^{c_1}$ is the final convolutional layer that acts as the final feature extractor, and \mathcal{N} is a nonlinear *activation function* [28]. In our case, we select \mathcal{N} as the *rectified linear unit (ReLU)*, which is defined as follows:

$$\mathcal{N}(x_1, x_2, \dots, x_n) = (\max(0, x_1), \max(0, x_2), \dots, \max(0, x_n)). \quad (24)$$

We send the output of the final residual block to a bilinear upsampling \mathcal{L} to expand the output dimension.

B.2. Inverse Problem DNN Architecture

Analogously as for the forward problem, we consider the following architecture:

$$\mathcal{F}_{\mathcal{R},\theta} := \mathcal{C}_{\theta_N} \circ \mathcal{S} \circ \mathcal{B}_{\theta_{N-1}}^{N-1} \circ \mathcal{B}_{\theta_{N-2}}^{N-2} \circ \dots \circ \mathcal{B}_{\theta_1}^1, \quad (25)$$

where $\theta = \{\theta_i : i = 1, \dots, N\}$ is a set of all the weights associated to each block and layer. In Equation (25), the residual blocks $\{\mathcal{B}_{\theta_i}^i : i = 1, \dots, 6\}$ are analogous to the ones in Equation (23), excluding the one dimensional upsampling. In this architecture, the convolutional layers perform the down-sampling. \mathcal{S} is a reshaping layer and \mathcal{C}_{θ_N} is a fully-connected layer, which performs the ultimate feature extraction and further down-sampling.

Using the above DNN architectures, minimization problems of Section 6 are optimized end-to-end with respect to ϕ and θ to obtain ϕ^* and θ^* .